Accepted Manuscript

Nonsingular Isogeometric Boundary Element Method for Stokes Flows in 3D
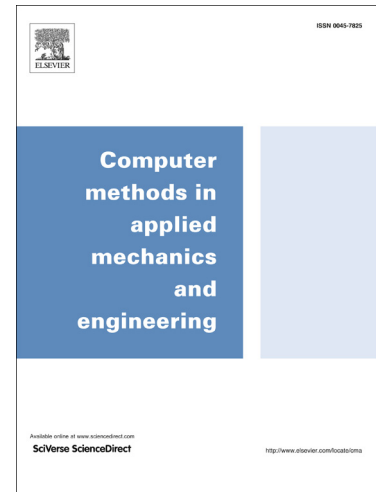
Luca Heltai, Marino Arroyo, Antonio DeSimone

Nonsingular Isogeometric Boundary Element Method for Stokes Flows in 3D

Luca Heltai[a,*], Marino Arroyo[b], Antonio DeSimone[a]

[a]*SISSA-International School for Advanced Studies*
Via Bonomea 265, 34136 Trieste - Italy
[b]*LaCàN, Dept. Applied Mathematics 3, Universitat Politècnica de Catalunya (UPC)*
Barcelona 08034, Spain

Abstract

Isogeometric analysis (IGA) is emerging as a technology bridging Computer Aided Geometric Design (CAGD), most commonly based on Non-Uniform Rational B-Splines (NURBS) surfaces, and engineering analysis. In finite element and boundary element isogeometric methods (FE-IGA and IGA-BEM), the NURBS basis functions that describe the geometry define also the approximation spaces. In the FE-IGA approach, the surfaces generated by the CAGD tools need to be extended to volumetric descriptions, a major open problem in 3D. This additional passage can be avoided in principle when the partial differential equations to be solved admit a formulation in terms of boundary integral equations, leading to Boundary Element Isogeometric Analysis (IGA-BEM). The main advantages of such an approach are given by the dimensionality reduction of the problem (from volumetric-based to surface-based), by the fact that the interface with CAGD tools is direct, and by the possibility to treat exterior problems, where the computational domain is infinite. By contrast, these methods produce system matrices which are full, and require the integration of singular kernels. In this paper we address the second point and propose a nonsingular formulation of IGA-BEM for 3D Stokes flows, whose convergence is carefully tested numerically. Standard Gaussian quadrature rules suffice to integrate the boundary integral equations, and carefully chosen known exact solutions of the interior Stokes problem are used to correct the resulting matrices, extending the work by Klaseboer et al. (Journal of Fluid Mechanics, 696(1):468–478, 2012) to IGA-BEM.

Keywords: Isogeometric Analysis, Boundary Element Method, Stokes Flows, NURBS

1. Introduction

Integration between finite element analysis (FEA) and conventional computer aided geometric design (CAGD) tools is becoming increasingly popular, following the isogeometric analysis (IGA) paradigm introduced by Hughes et al. in [24] for the discretization

---

*Corresponding author. Tel.: +39 040-3787449; Fax: +39 040-3787528
Email addresses: `luca.heltai@sissa.it` (Luca Heltai), `marino.arroyo@upc.edu` (Marino Arroyo), `antonio.desimone@sissa.it` (Antonio DeSimone)

of partial differential equations (PDEs). There are several motivations behind IGA techniques, the most prominent ones being related to the computational cost of translation of data between CAGD and FEA packages. The most attractive feature of IGA is its ability to maintain the same exact description of the computational domain geometry throughout the analysis process, by using the same class of functions used for geometry parameterization in CAGD packages, namely Non-Uniform Rational B-Splines (NURBS), for the PDE solution space. IGA is often seen as a generalization of standard FEMs, where more regular functions are employed. The additional regularity inherited from the NURBS spaces leads to other advantages with respect to FEA, such as better convergence properties and the ability to treat higher order problems (see, for example, the book by Cottrell et al. [14] for a comprehensive list of references on the argument).

While the finite element isogeometric analysis (FE-IGA) has received most of the attention of the scientific community, only few results are available for boundary element methods (BEM) and boundary integral equations (BIE) in general. In 2D, there are some works on potential flows, such as [36] and [44], and on elastostatic analysis [40]. Three dimensional applications are of great interest in the maritime community, and there are some works on NURBS based panel methods to study, for example, marine propellers [25] or the wavemaking resistance problem [10]. Three-dimensional IGA-BEM linear elasticity has recently been studied in [20] while some work on shape optimization has been presented in [29]. Boundary element isogeometric analysis (IGA-BEM) is very attractive for the solution of homogeneous elliptic PDEs, both in the interior and in the exterior cases, since it requires the solution of integral equations only on the boundary of the enclosing (or enclosed) domain, which is typically the only information that is generated by standard CAGD tools. In contrast, FE-IGA requires the extension of the computational domain inside (or outside) the enclosing CAGD surface, an outstanding problem in IGA.

While the dimensional reduction of the domain diminishes significantly both the number of degrees of freedom and the computational cost associated with the handling of the geometry, there are two main drawbacks which require special attention, and are common to all boundary integral discretizations: i) the system matrices that are produced with a boundary integral method are full, and ii) the integrands contain $(1/r)$ singularities or worse (in three dimensions) around the source point, arising from the fundamental solutions in formulating the boundary integrals. Both issues have perhaps contributed in keeping the IGA community away from boundary integral formulations.

In the literature, the first issue is usually tackled by acceleration techniques such as the fast multipole method [39] (see [31] for a survey of this technique applied to BEM), which allow one to solve the system without assembling the full matrices, and at the same time reduce the cost of the matrix-vector multiplication from $O(n^2)$ to $O(n)$ (this technique has already been applied to Laplace problems in two dimensional IGA-BEM in [44]). The second issue is more delicate and its solution depends highly on the degree of the discrete functional spaces and of the geometry description, remaining one of the most difficult aspects of the implementation of BEM. Different approaches are possible, (see, for example, [23]) but high order methods and curved geometries still remain challenging.

Popular approaches to tackle singular integration involve a local change of variables for the quadrature rules, following the principle that the Jacobian of the transformation can be used to eliminate locally the kernel singularities. Examples of these methods are given by Lachat and Watson [28] and by Telles [45]. Both methods are elegant and

2

produce accurate results, but they require a great number of basis functions evaluations, which need to be evaluated on different quadrature points whenever the element being integrated approaches a singularity.

Recently, Klaseboer et al. [26] proposed an analytical method that removes the singularities of the boundary integrals, by exploiting carefully chosen known solutions of the PDEs. These ideas, presented also in earlier theoretical works by Liu et al. [32, 30], were recently implemented for various elliptic PDEs in [27] and [43], and produce well conditioned boundary integrals, which can be integrated with standard quadrature rules.

In this paper we extend these ideas to isogeometric collocation boundary integral approximations of three-dimensional Stokes flow, and show once again the superior approximation properties of the isogeometric approach with respect to standard BEM implementations. The computational cost of this nonsingular method is much smaller when compared to traditional approximation procedures, and its accuracy is two to three orders of magnitude better than in the traditional isoparametric BEM when compared with the results presented in [43] for the same number of degrees of freedom. The improved performance obtained thanks to isogeometric analysis makes IGA-BEM a very promising tool for the solution of complex fluid-structure interaction problems arising in biophysics and bio-medical applications [15, 12]. In fact, our choice of Stokes flows as a model problem is motivated by our interest in modeling the flows induced by swimming bacteria and unicellular organisms [1, 4, 3, 2, 6] and lipid bilayer membranes [5, 38].

The rest of this paper is organized as follows. In Section 2 we present a brief overview of isogeometric NURBS spaces. The continuous problem that we want to takle by IGA-BEM is introduced in Section 3, while its boundary integral formulation is presented in Section 4. Section 5 is dedicated to the implementation details of the isogeometric collocation boundary element discretization of Stokes flow, and in Section 6 we present the generalization of the work by Klaseboerb et al.[26], [27] and [43]. Section 7 is dedicated to the numerical validation of the method presented in this paper and we draw some conclusions in Section 8.

2. Overview of isogeometric NURBS spaces

Given a nondecreasing knot vector $\Theta = \{k_0, k_1, ..., k_{n+p}\}$, the n basis splines of degree p are defined by the recurrence relation

$$B^{(i,0)}(s) = \begin{cases} 1, & \text{if } k_i \leq u < k_{i+1} \\ 0, & \text{otherwise,} \end{cases} \tag{1}$$

for $p = 0$, while for $p > 0$ we have

$$B^{(i,p)}(s) = \tau^{(i,p)}(s)B^{(i,p-1)}(s) - \tau^{(i+1,p)}(s)B^{(i+1,p-1)}(s), \tag{2}$$

for $i = 0, ..., n - 1$, where

$$\tau^{(i,p)}(s) := \begin{cases} \dfrac{s - k^i}{k^{i+p} - k^i} & \text{if } k^{i+p} \neq k^i \\ 0, & \text{otherwise.} \end{cases} \tag{3}$$

3

The above recurrence relation can be evaluated in a numerically stable way by the de Boor algorithm (see, for example, [35]). It is possible to generate a B-Spline curve $\boldsymbol{c}(s) \subset \Re^d$ by using a set of n coordinates $\boldsymbol{P}^i \in \Re^d$, referred to as *control points*, as

$$\boldsymbol{c}(s) = \sum_{i=0}^{n-1} \boldsymbol{P}^i B^{(i,p)}(s). \tag{4}$$

The properties of the curve $\boldsymbol{c}(s)$ depend highly on the properties of the knot vector Θ: if a knot is repeated q times, the curve $\boldsymbol{c}(s)$ at the location of the repeated knot is of class $\mathcal{C}^{p-q}$, and whenever a curve is only of class $\mathcal{C}^0$ at a knot location, then it is interpolatory at that location. Discontinuities ($\mathcal{C}^{-1}$ curves) are also allowed and are obtained when a knot is repeated $q = p+1$ times. Repeating a knot more than $p+1$ times is not allowed.

NURBS basis functions are readily obtained from B-Splines by assigning a positive weight w_i to each basis spline function and defining the corresponding NURBS basis function as

$$N^i(s) := \frac{w^i B^{(i,p)}(s)}{\sum_{j=0}^{n-1} w^j B^{(j,p)}(s)}. \tag{5}$$

Notice that also the NURBS basis have the partition of unity property, and B-Splines can be considered a special case of NURBS by taking all weights to be identical.

Taking m knot vectors Θ_i, with $i = 0, \ldots, m-1$, one can generalize the NURBS basis functions to m-dimensions by tensor products. Indicating with $\boldsymbol{s} := [s_0, ..., s_{m-1}] \in \Re^m$ a point in $\Re^m$ and $\boldsymbol{i} := (i_0, \ldots, i_{m-1})$ a multi-index belonging to the set

$$\mathcal{J} := \{\boldsymbol{j} = (j_1, \ldots, j_m), \quad 0 \le j_k < n_k, \quad k = 1, \ldots, m\}, \tag{6}$$

the m-variate B-Splines and NURBS basis functions are given by

$$B^{\boldsymbol{i},\boldsymbol{p}}(\boldsymbol{s}) := \prod_{k=0}^{m-1} B^{(i_k,p_k)}(s_k), \qquad N^{\boldsymbol{i}}(\boldsymbol{s}) := \frac{w_{\boldsymbol{i}} B^{(\boldsymbol{i},\boldsymbol{p})}(\boldsymbol{s})}{\sum_{\boldsymbol{j} \in \mathcal{J}} w^{\boldsymbol{j}} B^{(\boldsymbol{j},\boldsymbol{p})}(\boldsymbol{s})}, \tag{7}$$

where $\boldsymbol{i}$, $\boldsymbol{p}$ and $\boldsymbol{j}$ are all multi-indices. The multi-index $\boldsymbol{p} = (p_0, \ldots, p_{m-1})$ is used to keep track of the degrees of the B-Splines in each direction, while $\boldsymbol{n} = (n_0, \ldots, n_{k-1})$ is used to keep track of the number of basis functions in each direction. Notice that in Equations (5) and (7) we dropped the superscripts p and $\boldsymbol{p}$ from the definition of the NURBS basis functions N^i, to ease the notation in the rest of the paper.

As a generalization of the one dimensional case, if we take a collection of $n := \prod_{k=0}^{m-1} n_k$ control points in $\Re^d$, with $d \ge m$, we can represent a m-dimensional manifold in a d-dimensional space as the image of the map

$$\Re^d \supset \boldsymbol{x}(\boldsymbol{s}) := \sum_{\boldsymbol{i} \in \mathcal{J}} \boldsymbol{P}^{\boldsymbol{i}} N^{\boldsymbol{i}}(\boldsymbol{s}) \qquad \boldsymbol{s} \in \Re^m. \tag{8}$$

When m is equal to one two or three, the set of control points $\boldsymbol{P}^{\boldsymbol{i}}$ with $\boldsymbol{i} \in \mathcal{J}$ is referred to as *control polygon*, *control net* or *control lattice* respectively. The domain of the map $\boldsymbol{x}(\boldsymbol{s})$ is the set

$$B^m := [k_0^0, k_{n_1+p_1}^0] \times \cdots \times [k_0^{m-1}, k_{n_{m-1}+p_{m-1}}^{m-1}] \subset \Re^m, \tag{9}$$

4

where k_j^i is the j-th knot in the i-th knot vector Θ_i. The first fundamental form associated to the map $\boldsymbol{x}(\boldsymbol{s})$ is given by

$$g(\boldsymbol{s}) := (D\boldsymbol{x}(\boldsymbol{s}))^T D\boldsymbol{x}(\boldsymbol{s}) \qquad \in \Re^{m \times m}, \tag{10}$$

where $D\boldsymbol{x}(\boldsymbol{s})$ is the Jacobian of the mapping $\boldsymbol{x}(\boldsymbol{s})$:

$$(D\boldsymbol{x}(\boldsymbol{s}))_{ab} := \frac{\partial \boldsymbol{x}_a}{\partial \boldsymbol{s}_b}(\boldsymbol{s}) = \sum_{\boldsymbol{k} \in \mathcal{J}} (\boldsymbol{P^k} \cdot \boldsymbol{e}_a) \frac{\partial N^{\boldsymbol{k}}}{\partial \boldsymbol{s}_b}(\boldsymbol{s}),$$
$$a = 0, \ldots, d-1 \qquad b = 0, \ldots, m-1, \tag{11}$$

$\boldsymbol{e}_a$ is a unit vector in the a-th spatial direction, and $\boldsymbol{k}$ is a multi-index.

Integrals on the m-dimensional manifold $\boldsymbol{x}(B^m)$ can be pulled back to the domain B^m using the standard transformation rule

$$\int_{\boldsymbol{x}(B^m)} f(\boldsymbol{x}) \, \mathrm{d}\gamma^m = \int_{B^m} f(\boldsymbol{x}(\boldsymbol{s})) J(\boldsymbol{s}) \, \mathrm{d}\boldsymbol{s}, \tag{12}$$

where we indicated with $J(\boldsymbol{s})$ the square root of the determinant of the first fundamental form:

$$J(\boldsymbol{s}) := \sqrt{\det(g(\boldsymbol{s}))}. \tag{13}$$

The geometry $\Omega \equiv \boldsymbol{x}(B^d)$ of the domain or of its boundary Γ can then be represented via the NURBS basis above, by choosing appropriately the knot spans, the weights and the control points that define the mapping $\boldsymbol{x}(\boldsymbol{s})$. A geometry based on the map defined above is referred to as *CAGD patch*. The full domain Ω may be constructed by gluing together several patches. For the sake of simplicity, however, we expose the theory and the numerical approximation only considering *single patch geometries*, referring to [14] for treatments of multi-patch domains, with different level of regularity across different patches, as well as for indications on how to treat different refinements on each patch.

A standard (scalar) isogeometric finite dimensional space is readily obtained by considering the span of the functions $\phi^{\boldsymbol{i}} := N^{\boldsymbol{i}} \circ \boldsymbol{x}^{-1}$:

$$V_h := \mathrm{span}\{\phi^{\boldsymbol{i}}(\boldsymbol{y})\}_{\boldsymbol{i} \in \mathcal{J}}, \qquad \boldsymbol{y} \in \boldsymbol{x}(B^m) \subset \Re^d, \tag{14}$$

where $\phi^{\boldsymbol{i}}$ are such that

$$\phi^{\boldsymbol{i}}(\boldsymbol{x}(\boldsymbol{s})) = N^{\boldsymbol{i}}(\boldsymbol{s}), \qquad \forall \boldsymbol{s} \in B^m. \tag{15}$$

The dimension of the space V_h is $n = \prod_{k=1}^{m} n_k$ and it is equal to the number of control points that define the geometry of the problem. A finite dimensional space for vector fields of q components is obtained by considering

$$V_h^q := \mathrm{span}\{\boldsymbol{\tau}^i(\boldsymbol{y})\}_{i=1}^{qn} \qquad \boldsymbol{y} \in \boldsymbol{x}(B^m) \subset \Re^d, \tag{16}$$

where the basis functions $\boldsymbol{\tau}^i$ are such that

$$\boldsymbol{\tau}^i(\boldsymbol{y}) := \boldsymbol{e}_a \phi^{\boldsymbol{j}}(\boldsymbol{y}), \qquad n_{-1} := 1, \quad i = q \left(\sum_{w=0}^{m-1} \left(j_w \prod_{k=0}^{w-1} n_{k-1} \right) \right) + a. \tag{17}$$

5

The global index i varies continuously from one to $qn = q \prod_{k=1}^{m} n_k$, and it is meant to transform the multi-index $\boldsymbol{j} \in \mathcal{J}$ plus the component index a into a unique global identifier for the i-th basis function. Conversely, given a global index j, it is possible to infer to which component the basis function refers to, and what is the multi-index which identifies the underlying NURBS basis by inverting the rightmost expression in Equation (17).[1]

In what follows, we use upper latin indices starting from i to indicate the global numbering of the basis functions defining the space V_h^q and lower latin indices starting from a to label spacial coordinates. For spatial coordinates, we use Einstein summation convention. A vector function of q components $\boldsymbol{f}(\boldsymbol{x})$ in the space V_h^q is identified by its coefficient vector $\boldsymbol{f}$ such that

$$V_h^q \ni \boldsymbol{f}(\boldsymbol{x}) := \sum_{i=0}^{nq-1} f^i \boldsymbol{\tau}^i(\boldsymbol{x}), \tag{18}$$

where, with a slight abuse of notation, we denote the vector of coefficients $\boldsymbol{f}$ with the same symbol as the function $\boldsymbol{f}(\boldsymbol{x})$ but without the argument "$(\boldsymbol{x})$".

Finite element isogeometric analysis (FE-IGA) is based on functional spaces V_h in which the dimension m of the reference manifold B^m and of embedding space $\Re^d$ are equal, i.e., $m = d$.

Boundary integral equations, on the other hand, rely on the convolution with fundamental solutions to study the problem only on the *boundary* Γ of the domain Ω, requiring a discretization of functional spaces defined on manifolds of co-dimension one, i.e., $m = d - 1$.

3. Hydrodynamic equations

We are interested in solving Stokes equations in a domain $\tilde{\Omega} \subseteq \Re^d$, with a given Dirichlet boundary condition $\boldsymbol{u}_g$ on $\tilde{\Gamma} := \partial\tilde{\Omega}$, and d is either two or three. Neumann or mixed problems can be treated in a similar way (see, for example,[22]), and we use this model system simply to fix the ideas.

In both the finite and infinite domain cases, we will study problems for which it is possible to identify a closed domain Ω, that is used to generate the domain of the fluid $\tilde{\Omega}$ and its boundary $\tilde{\Gamma}$. In the exterior case, we have that $\tilde{\Omega} := \Re^d \setminus \overline{\Omega}$, while in the interior case, $\tilde{\Omega} \equiv \Omega$.

With this convention, the interior and the exterior Stokes problems can both be expressed by the following set of equations:

$$-\eta\Delta\boldsymbol{u} + \nabla p = -\nabla \cdot \boldsymbol{\sigma} = 0 \qquad \text{in } \tilde{\Omega} \tag{19a}$$

$$\nabla \cdot \boldsymbol{u} = 0 \qquad \text{in } \tilde{\Omega} \tag{19b}$$

$$\boldsymbol{u} = \boldsymbol{u}_g \qquad \text{on } \tilde{\Gamma} \tag{19c}$$

---

[1]For example, in Matlab the local to global conversion is obtained with the function SUB2IND, while the global to local conversion is obtained by the function IND2SUB.

6

where $\boldsymbol{u}$ and p are the velocity and hydrodynamic pressure fields in the domain $\tilde{\Omega}$ (either finite or infinite), η is the viscosity of the fluid, $\boldsymbol{u}_g$ is the (given) fluid velocity at the boundary of the domain and $\boldsymbol{\sigma}$ is the Cauchy stress tensor for an incompressible Newtonian fluid:

$$\boldsymbol{\sigma} := -p\boldsymbol{I} + \eta(\nabla\boldsymbol{u} + \nabla\boldsymbol{u}^T). \tag{20}$$

Equations (19a) and (19b) describe the conservation of linear momentum and mass in the Stokes fluid, while (19c) is a Dirichlet boundary condition. The pressure p can be regarded as the Lagrange multiplier associated with the conservation of volume (19b), and it is uniquely determined by $\boldsymbol{u}$ up to an additive constant.

When the domain is infinite, i.e., when we are treating the exterior Stokes problem, then the boundary $\tilde{\Gamma}$ is split into two parts: the boundary Γ of the finite domain Ω, and the boundary at infinity, Γ_∞, defined as

$$\Gamma_\infty := \lim_{R\to\infty} \partial B_R(0), \tag{21}$$

where $B_R(0)$ is the ball of radius R centered at the origin.

In the infinite domain case, System (19) has a unique solution in the Sobolev spaces $H^1(\tilde{\Omega})$ for the velocity and $L_0^2(\tilde{\Omega})$ for the pressure (here the subscript zero stands for zero mean average), provided that the Dirichlet boundary data $\boldsymbol{u}_g$ goes to zero sufficiently fast on Γ_∞, that its portion on Γ is in the space $H^{\frac{1}{2}}(\Gamma)$, and provided that Γ is regular enough. A boundary Γ of class $\mathcal{C}^1$ guarantees existence and uniqueness of the exterior solution $\boldsymbol{u}$, see, for example Ref. [17].

For the finite domain case to have a solution, the Dirichlet data $\boldsymbol{u}_g$ needs to be compatible with the mass conservation equation, i.e.,

$$(\boldsymbol{u}_g, \boldsymbol{n}) := \int_\Gamma \boldsymbol{u}_g \cdot \boldsymbol{n}\, \mathrm{d}\Gamma = 0, \tag{22}$$

where $\boldsymbol{n}$ is the outer normal to the domain Ω, and the notation $(\cdot, \cdot)$ is used for the $L^2(\Gamma)^d$ inner product. Also in the interior case, a boundary Γ of class $\mathcal{C}^1$ and boundary data $\boldsymbol{u}_g \in H^{\frac{1}{2}}(\Gamma)$, satisfying (22), guarantee existence and uniqueness of a solution.

4. Boundary integral representation

Our boundary integral formulation follows closely Ref. [37] and Ref [42]: if we consider Stokes equation in free-space associated with a forcing term due to a Dirac mass centered in $\boldsymbol{y}$ and weighted with the force vector $\boldsymbol{k}$, i.e.,

$$\begin{aligned}
-\eta\Delta\boldsymbol{u}(\boldsymbol{x}) + \nabla p(\boldsymbol{x}) = -\nabla\cdot\boldsymbol{\sigma} &= \boldsymbol{k}\delta(\boldsymbol{x} - \boldsymbol{y}) &&\text{in } \Re^d \\
\nabla\cdot\boldsymbol{u}(\boldsymbol{x}) &= 0 &&\text{in } \Re^d \\
\lim_{|\boldsymbol{x}|\to\infty} |\boldsymbol{u}(\boldsymbol{x})| &= 0 \\
\lim_{|\boldsymbol{x}|\to\infty} |p(\boldsymbol{x})| &= 0,
\end{aligned} \tag{23}$$

7

we can express the solution $\boldsymbol{u}$ and $\boldsymbol{\sigma}$ using the free-space Green's functions $\boldsymbol{\mathcal{S}}$ and $\boldsymbol{\mathcal{T}}$:

$$u_a(\boldsymbol{x}) = \frac{1}{4(d-1)\pi\eta}\mathcal{S}_{ab}(\boldsymbol{x}-\boldsymbol{y})k_b$$

$$\sigma_{ac}(\boldsymbol{x}) = \frac{1}{4(d-1)\pi}\mathcal{T}_{abc}(\boldsymbol{x}-\boldsymbol{y})k_b, \tag{24}$$

where

$$\mathcal{S}_{ab}(\boldsymbol{r}) = \frac{r_a r_b}{|\boldsymbol{r}|^d} + \begin{cases} -\delta_{ab}\log(|\boldsymbol{r}|) & \text{if } d=2 \\ \frac{\delta_{ab}}{|\boldsymbol{r}|} & \text{if } d=3 \end{cases}$$

$$\mathcal{T}_{abc}(\boldsymbol{r}) = -2d\frac{r_a r_b r_c}{|\boldsymbol{r}|^{d+2}}. \tag{25}$$

When Γ is Lipschitz regular, we can define the single and double layer potentials:

$$\tilde{\boldsymbol{\mathcal{D}}} : H^{-\frac{1}{2}}(\Gamma)^d \longrightarrow H^1(\Re^d \setminus \Gamma)^d$$

$$(\tilde{\boldsymbol{\mathcal{D}}}\boldsymbol{f})_a(\boldsymbol{x}) := \frac{1}{4(d-1)\pi\eta}\int_\Gamma \mathcal{S}_{ab}(\boldsymbol{x}-\boldsymbol{y})f_b(\boldsymbol{y})\,\mathrm{d}\Gamma(\boldsymbol{y}) \tag{26}$$

$$\tilde{\boldsymbol{\mathcal{N}}} : H^{\frac{1}{2}}(\Gamma)^d \longrightarrow H^1(\Re^d \setminus \Gamma)^d$$

$$(\tilde{\boldsymbol{\mathcal{N}}}\boldsymbol{u})_a(\boldsymbol{x}) := \frac{1}{4(d-1)\pi}\int_\Gamma^{PV} \mathcal{T}_{abc}(\boldsymbol{x}-\boldsymbol{y})u_b(\boldsymbol{y})n_c(\boldsymbol{y})\,\mathrm{d}\Gamma(\boldsymbol{y}). \tag{27}$$

Although the integral in Equation (27) is well defined for each $\boldsymbol{x}$ in $\Re^d \setminus \Gamma$, we retain the PV symbol to indicate an integral in the Cauchy principal value sense, to maintain the same definition of $\tilde{\boldsymbol{\mathcal{N}}}$ when taking its trace on Γ, later in this section. Indeed, given the solution $\boldsymbol{u} \in H^1(\tilde{\Omega})^d$ of System (19), and its associated stress tensor $\boldsymbol{\sigma} \in L^2(\tilde{\Omega})^{d\times d}$, we have a boundary integral representation of the solution $\boldsymbol{u}$ in arbitrary points $\boldsymbol{x} \in \tilde{\Omega}$ in terms of the traces of $\boldsymbol{u}$ and $\boldsymbol{\sigma}\boldsymbol{n}$ on Γ (see, for example, [37] or [42]).

Calling $\gamma_0^{int} : H^s(\Gamma)^d \to H^{s-\frac{1}{2}}(\Gamma)^d$ and $\gamma_0^{ext} : H^s(\Gamma)^d \to H^{s-\frac{1}{2}}(\Gamma)^d$ the interior and exterior trace operators (when Γ is a Lipschitz boundary we can choose s in $\Re$ [17]), and defining $\boldsymbol{u}^{int/ext} := \gamma_0^{int/ext}\boldsymbol{u}$, and $\boldsymbol{\sigma}^{int/ext}\boldsymbol{n} := \gamma_0^{int/ext}\boldsymbol{\sigma}\boldsymbol{n}$ we have

$$\boldsymbol{u}(\boldsymbol{x}) + (\tilde{\boldsymbol{\mathcal{N}}}\boldsymbol{u}^{int})(\boldsymbol{x}) = +\left(\tilde{\boldsymbol{\mathcal{D}}}(\boldsymbol{\sigma}^{int}\boldsymbol{n})\right)(\boldsymbol{x}), \qquad\qquad \boldsymbol{x} \in \Omega \tag{28}$$

$$\boldsymbol{u}(\boldsymbol{x}) - (\tilde{\boldsymbol{\mathcal{N}}}\boldsymbol{u}^{ext})(\boldsymbol{x}) = -\left(\tilde{\boldsymbol{\mathcal{D}}}(\boldsymbol{\sigma}^{ext}\boldsymbol{n})\right)(\boldsymbol{x}), \qquad\qquad \boldsymbol{x} \in \Re^d \setminus \overline{\Omega}. \tag{29}$$

Equation (28) is the boundary integral representation for an interior Stokes flow, where the trace $\boldsymbol{u}^{int}$ of $\boldsymbol{u}$ on Γ has to satisfy condition (22), while Equation (29) is the boundary integral representation for an exterior Stokes flow, where the trace $\boldsymbol{u}^{ext}$ on Γ is allowed to be arbitrary, as long as it belongs to the space $H^{\frac{1}{2}}(\Gamma)$.

Notice that in the infinite domain case, both integrals on Γ_∞ disappear due to boundary conditions, and the distinction between the interior and the exterior case in Equations (28) and (29) is only given by the signs in front of the single and double layer potentials, which take into account the fact that the normal $\boldsymbol{n}$ is pointing outwards with

8

respect to the domain Ω; therefore, it is inward with respect to the domain of integration in the exterior case.

Since both the single and the double layer operators have their range in $H^1(\Re^d \setminus \Gamma)$, we can take the interior trace on Γ in Equation (28) and the exterior trace on Γ in Equation (29) to obtain boundary integral equations defined on Γ only. When taking the traces of the single layer potential, the integral in Equation (26) becomes weakly singular but remains integrable, and it is continuous across Γ. On the contrary the integration of the double layer potential only converges in the Cauchy principal value sense, and it jumps across Γ. We define the single and double layer operators respectively as:

$$\boldsymbol{\mathcal{D}} := \gamma_0^{int}\tilde{\boldsymbol{\mathcal{D}}} = \gamma_0^{ext}\tilde{\boldsymbol{\mathcal{D}}} \qquad\qquad : H^{-\frac{1}{2}}(\Gamma)^d \quad \rightarrow \quad H^{\frac{1}{2}}(\Gamma)^d \qquad (30)$$

$$\boldsymbol{\mathcal{N}} := (1-c)\boldsymbol{I} + \gamma_0^{int}\tilde{\boldsymbol{\mathcal{N}}} = c\boldsymbol{I} + \gamma_0^{ext}\tilde{\boldsymbol{\mathcal{N}}} \qquad : H^{\frac{1}{2}}(\Gamma)^d \quad \rightarrow \quad H^{\frac{1}{2}}(\Gamma)^d, \qquad (31)$$

where $\boldsymbol{I}$ is the identity and the scalar function $c(\boldsymbol{x})$ is defined as

$$c(\boldsymbol{x}) := \lim_{\varepsilon \to 0} \frac{\int_{\Omega \cap \partial B_\varepsilon(\boldsymbol{x})} \mathrm{d}\Gamma}{2(d-1)\pi\varepsilon^2} = \begin{cases} 1 & \text{if } \boldsymbol{x} \in \Omega \\ \dfrac{1}{2} & \text{if } \boldsymbol{x} \in \Gamma \text{ of class } \mathcal{C}^1 \\ 0 & \text{if } \boldsymbol{x} \in \Re^d \setminus \overline{\Omega}, \end{cases} \qquad (32)$$

and it is there to take into account the Cauchy limiting value of the double layer integral (see, for example, [42]). In general $c(\boldsymbol{x})$ is the fraction of angle ($d = 2$) or solid angle ($d = 3$) from which the domain Ω is seen by $\boldsymbol{x} \in \Gamma$ and it is almost everywhere equal to $1/2$ for a Lipschitz boundary.

Although in the Sobolev space $H^{\frac{1}{2}}(\Gamma)^d$ we could drop the function c and use directly the value $1/2$ (as it is often done in the literature), we retain the function c itself in view of the numerical discretization by collocation boundary element methods, in which a correct evaluation of c at corners and edges of the integration domain Γ is essential for accurate numerical results. The interior and exterior Stokes problems satisfy the boundary integral equations

$$c\boldsymbol{u}^{int} + \boldsymbol{\mathcal{N}}\boldsymbol{u}^{int} = \boldsymbol{\mathcal{D}}\boldsymbol{f}^{int} \qquad \text{in } H^{\frac{1}{2}}(\Gamma) \qquad\qquad (33)$$

$$(1-c)\boldsymbol{u}^{ext} - \boldsymbol{\mathcal{N}}\boldsymbol{u}^{ext} = \boldsymbol{\mathcal{D}}\boldsymbol{f}^{ext} \qquad \text{in } H^{\frac{1}{2}}(\Gamma), \qquad\qquad (34)$$

where $\boldsymbol{f}^{int} := \boldsymbol{\sigma}^{int}\boldsymbol{n}$ and $\boldsymbol{f}^{ext} := \boldsymbol{\sigma}^{ext}\boldsymbol{n}^{ext} = -\boldsymbol{\sigma}^{ext}\boldsymbol{n}$ are the interior and exterior normal tractions on Γ.

Solving Stokes problem for both the interior and the exterior case simultaneously, and summing Equations (33) and (34) one obtains the following compact representation integral, also known as Stokes transmission problem:

$$\{\!\!\{\boldsymbol{u}\}\!\!\}_c + \boldsymbol{\mathcal{N}}[\![\boldsymbol{u}]\!] = \boldsymbol{\mathcal{D}}[\![\boldsymbol{\sigma}]\!]\boldsymbol{n} \qquad\qquad (35)$$

where $\{\!\!\{\cdot\}\!\!\}_c$ and $[\![\cdot]\!]$ are the *c-weighted average* and *jump* operators, defined as

$$\{\!\!\{a\}\!\!\}_c := \left(ca^{int} + (1-c)a^{ext}\right)$$
$$[\![a]\!] := \left(a^{int} - a^{ext}\right).$$

Boundedness of the single and double layer operators can be shown when Γ is the boundary of a Lipschitz domain Ω:

$$\begin{aligned}
\boldsymbol{\mathcal{D}} &: H^{-\frac{1}{2}+s}(\Gamma)^d &\to H^{\frac{1}{2}+s}(\Gamma)^d \\
\boldsymbol{\mathcal{N}} &: H^{\frac{1}{2}+s}(\Gamma)^d &\to H^{\frac{1}{2}+s}(\Gamma)^d,
\end{aligned} \tag{36}$$

for all $|s| \leq \frac{1}{2}$ (see, for example, [42]).

Some properties of the single layer operator can be inferred from the consideration that $\boldsymbol{u} = 0, p = -1$ is a solution to Problem (19), both in the interior and the exterior case. Plugging this solution into Equation (33) or (34) we obtain

$$\boldsymbol{\mathcal{D}}\boldsymbol{n} = 0, \tag{37}$$

and it is possible to show (see, for example, [17]) that the single layer potential $\boldsymbol{\mathcal{D}}$ is elliptic in the subspace $H_*^{-\frac{1}{2}}(\Gamma)^d$ defined as

$$H_*^{-\frac{1}{2}}(\Gamma)^d := \left\{ \boldsymbol{w} \in H^{-\frac{1}{2}}(\Gamma)^d \text{ s.t. } <\boldsymbol{w}, \boldsymbol{n}> := \int_\Gamma \boldsymbol{w} \cdot \boldsymbol{n} = 0 \right\}, \tag{38}$$

where the notation $< \cdot, \cdot >$ is used to indicate the duality between $H^{-\frac{1}{2}}(\Gamma)^d$ and $H^{\frac{1}{2}}(\Gamma)^d$, in contrast with $(\cdot, \cdot)$ which is used for the $L^2(\Gamma)^d$ inner product.

If we consider the interior problem only, then the homogeneous Neumann problem ($\boldsymbol{f}^{int} = 0$) has non trivial solutions corresponding to the the $3(d-1)$ dimensional space of rigid body velocities $\mathcal{R}$.[2] Plugging these solutions into Equation (33), we get

$$\boldsymbol{\mathcal{N}}\boldsymbol{u}_R = -c\boldsymbol{u}_R \qquad \forall \boldsymbol{u}_R \in \mathcal{R}, \tag{39}$$

and one can show ellipticity of the operator $c\boldsymbol{I} + \boldsymbol{\mathcal{N}}$ in the subspace $H_R^{\frac{1}{2}}(\Gamma)^d$, defined as

$$H_R^{\frac{1}{2}}(\Gamma)^d := \left\{ \boldsymbol{v} \in H^{\frac{1}{2}}(\Gamma)^d \text{ s.t. } (\boldsymbol{v}, \boldsymbol{u}_R) = 0, \quad \forall \boldsymbol{u}_R \in \mathcal{R} \right\}. \tag{40}$$

Since the operator $\boldsymbol{\mathcal{D}}$ has a nonempty kernel, we can incorporate the eigenspace to obtain uniquely solvable boundary integral integrations (see, for example, [22]). At the discrete level this is necessary to make the inversion of the discrete version of operator $\boldsymbol{\mathcal{D}}$ well conditioned.

We introduce the extended operator $\overline{\boldsymbol{\mathcal{D}}}$ defined as

$$< \overline{\boldsymbol{\mathcal{D}}}\boldsymbol{f}, \boldsymbol{u} > := < \boldsymbol{\mathcal{D}}\boldsymbol{f}, \boldsymbol{u} > + \gamma < \boldsymbol{f}, \boldsymbol{n} > (\boldsymbol{u}, \boldsymbol{n})$$
$$\forall \boldsymbol{u} \in H^{\frac{1}{2}}(\Gamma)^d, \quad \forall \boldsymbol{f} \in H^{-\frac{1}{2}}(\Gamma)^d, \qquad \gamma \geq 0, \quad (41)$$

which, by definition, coincides with $\boldsymbol{\mathcal{D}}$ in the space $H_*^{-\frac{1}{2}}(\Gamma)^d$. In the operator $\overline{\boldsymbol{\mathcal{D}}}$, the zeroth eigenvalue of $\boldsymbol{\mathcal{D}}$ (corresponding to the eigenvector $\boldsymbol{n}$) is substituted with $\gamma/(\boldsymbol{n}, \boldsymbol{n})$.

---

[2]When $d = 2$, $\mathcal{R} := \text{span}\left\{ \begin{pmatrix} 1 \\ 0 \end{pmatrix}, \begin{pmatrix} 0 \\ 1 \end{pmatrix}, \begin{pmatrix} -y \\ x \end{pmatrix} \right\}$, while when $d = 3$ we have that $\mathcal{R} :=$ $\text{span}\left\{ \begin{pmatrix} 1 \\ 0 \\ 0 \end{pmatrix}, \begin{pmatrix} 0 \\ 1 \\ 0 \end{pmatrix}, \begin{pmatrix} 0 \\ 0 \\ 1 \end{pmatrix}, \begin{pmatrix} -y \\ x \\ 0 \end{pmatrix}, \begin{pmatrix} 0 \\ -z \\ y \end{pmatrix}, \begin{pmatrix} z \\ 0 \\ -x \end{pmatrix} \right\}$.

10

A positive γ ensures invertibility of the Dirichlet matrix in the finite dimensional spaces approximating $H^{\frac{1}{2}}(\Gamma)^d$ and $H^{-\frac{1}{2}}(\Gamma)^d$.

The extended operator $\overline{\boldsymbol{\mathcal{D}}}$ can be used to define two Dirichlet to Neumann maps, DN_Γ^{int} and DN_Γ^{ext}, where the Dirichlet data $\boldsymbol{u}_g$ is given, and we want to find out the tractions $\boldsymbol{f} := \boldsymbol{\sigma n} = DN_\Gamma \boldsymbol{u}_g$ on Γ. In both cases we obtain Fredholm integral equations of the first kind given by

$$
\begin{aligned}
DN_\Gamma^{int} &:= \overline{\boldsymbol{\mathcal{D}}}^{-1}(c\boldsymbol{I} + \boldsymbol{\mathcal{N}}) \\
DN_\Gamma^{ext} &:= \overline{\boldsymbol{\mathcal{D}}}^{-1}\big((1-c)\boldsymbol{I} - \boldsymbol{\mathcal{N}}\big).
\end{aligned}
\tag{42}
$$

We remark here that in the Dirichlet to Neumann maps of Equation (42), the extended operator $\overline{\boldsymbol{\mathcal{D}}}$ will provide specific uniquely determined solutions of the integral equations, whereas the original Stokes Dirichlet problem still has the null space span($\boldsymbol{n}$) (see, for example, [22]).

Among all possible Neumann solutions (which are not unique, since the pressure is known up to a constant), the ones which are selected by the Dirichlet to Neumann maps (42) are those for which the normal traction $\boldsymbol{f}$ is in the space $H^{-\frac{1}{2}}(\Gamma)_*^d$.

An effective way to discretize the boundary integral equations (33) and (34) and the resulting maps given in Equation (42) is given by the boundary element method, in which $\boldsymbol{u}$ and $\boldsymbol{f}$ are sought for in a finite dimensional space defined on Γ, and the Dirichlet to Neumann maps become matrices.

Here we exploit the isogeometric NURBS spaces defined in Section 2 to define the finite dimensional spaces, as well as the discrete versions of the boundary integral equations (33) and (34) and of the Dirichlet to Neumann maps (42). The integration in both operators is desingularized extending the techniques introduced in [27, 26, 43] for standard boundary element methods to the isogeometric approximation introduced here.

5. Isogeometric collocation BEM for Stokes flows

We assume the boundary Γ of the domain Ω to be a closed curve if $d = 2$ or a closed surface if $d = 3$. Once a CAGD description of Γ is available, we can readily define the isogeometric vector space $V_h^d(\Gamma)$ of finite dimensional functions of d components defined on Γ using the tools introduced in Section 2.

When the boundary Γ is piecewise smooth (and therefore also the finite dimensional space $V_h^d(\Gamma)$ is piecewise smooth), we can exploit the higher regularity for the velocity fields and for the normal traction fields and the boundedness of the single and double layer operators expressed in Equation (36) to give sense to point-wise evaluation of the single and double layer operators defined in Equations (30) and (31).

This process allows one to obtain square matrices that approximate the single and double layer operators, by *collocating* the boundary integral equations (33) or (34) at n distinct *collocation points* $\{\boldsymbol{x}^\alpha\}_{\alpha=1}^n$, and restricting both $\boldsymbol{u}(\boldsymbol{x})$ and $\boldsymbol{f}(\boldsymbol{x})$ to live in the finite dimensional space $V_h^d(\Gamma) \subset H^{\frac{1}{2}}(\Gamma)^d \subset H^{-\frac{1}{2}}(\Gamma)^d$:

$$
c(\boldsymbol{x}^\alpha)\boldsymbol{u}^{int,j}\boldsymbol{\tau}^j(\boldsymbol{x}^\alpha) + \big(\boldsymbol{\mathcal{N}}\boldsymbol{u}^{int,j}\boldsymbol{\tau}^j\big)(\boldsymbol{x}^\alpha) = \big(\boldsymbol{\mathcal{D}}\boldsymbol{f}^{int,j}\boldsymbol{\tau}^j\big)(\boldsymbol{x}^\alpha)
\tag{43}
$$

$$
\big(1 - c(\boldsymbol{x}^\alpha)\big)\boldsymbol{u}^{ext,j}\boldsymbol{\tau}^j(\boldsymbol{x}^\alpha) - \big(\boldsymbol{\mathcal{N}}\boldsymbol{u}^{ext,j}\boldsymbol{\tau}^j\big)(\boldsymbol{x}^\alpha) = \big(\boldsymbol{\mathcal{D}}\boldsymbol{f}^{ext,j}\boldsymbol{\tau}^j\big)(\boldsymbol{x}^\alpha)
\tag{44}
$$

11

where summation is implied over j. In what follow we use greek upper indices to indicate an index running from zero to $n-1$, identifying a specific collocation point $\boldsymbol{x}^{\alpha}$. For each collocation point $\boldsymbol{x}^{\alpha}$, Equations (43) and (44) are systems of d equations in $2dn$ unknowns (the dn coefficients of $\boldsymbol{u}$ and the dn coefficients of $\boldsymbol{f}$), which can be compactly rewritten as

$$CM\boldsymbol{u}^{int} + N\boldsymbol{u}^{int} = \boldsymbol{D}\boldsymbol{f}^{int} \tag{45}$$

$$(I-C)M\boldsymbol{u}^{ext} - N\boldsymbol{u}^{ext} = \boldsymbol{D}\boldsymbol{f}^{ext}, \tag{46}$$

where the (square) matrices $\boldsymbol{M}$, $\boldsymbol{N}$, $\boldsymbol{D}$ and C are given by

$$\boldsymbol{M}^{(\alpha d+a)\,(j)} := \delta_{ab}\tau_b^j(\boldsymbol{x}^{\alpha}) \tag{47}$$

$$\boldsymbol{N}^{(\alpha d+a)\,(j)} := \frac{1}{4(d-1)\pi} \int_{\Gamma} \mathcal{T}_{abc}(\boldsymbol{x}^{\alpha} - \boldsymbol{y})\tau_b^j(\boldsymbol{y})n_c(\boldsymbol{y})\,\mathrm{d}\Gamma_y \tag{48}$$

$$\boldsymbol{D}^{(\alpha d+a)\,(j)} := \frac{1}{4(d-1)\pi\eta} \int_{\Gamma} \mathcal{S}_{ab}(\boldsymbol{x}^{\alpha} - \boldsymbol{y})\tau_b^j(\boldsymbol{y})\,\mathrm{d}\Gamma_y \tag{49}$$

$$C^{ij} := -\delta_{ij}\frac{\sum_{k=0}^{dn-1}\boldsymbol{N}^{ik}}{\sum_{k=0}^{dn-1}\boldsymbol{M}^{ik}} = -\delta_{ij}\sum_{k=0}^{dn-1}\boldsymbol{N}^{ik} \tag{50}$$

and the index α runs from zero to $n-1$, a,b,c run from zero to $d-1$ and j runs from zero to $dn-1$. Summation is implied over the spatial coordinate indices a,b,c and δ_{ij} is the Kronecker delta, which is one if i is equal to j, and zero otherwise.

Equation (50) is a numerical way to compute the fraction of solid angle by which the collocation points $\boldsymbol{x}^{\alpha}$ see the domain. This technique is usually known as the Rigid Body Mode (RBM) or rigid mode technique (see, for example, [16]), and it exploits the boundary integral identity (39) for rigid modes to compute exactly the coefficients $c(\boldsymbol{x}^{\alpha})$.

A common approach for the choice of the collocation points is given by the Greville abscissæ (see, for example, [19], or [8]), which are defined as

$$\boldsymbol{x}^{\alpha} := \boldsymbol{x}(\boldsymbol{s}^{\alpha}), \qquad \boldsymbol{s}^{\alpha_i} := \frac{\sum_{j=1}^{p} k_{\alpha_i+j}^i}{p}, \tag{51}$$

where $\boldsymbol{\alpha}$ is the multi-index associated with the linear global index α and $k_{\alpha_i+j}^i$ are the knots of the knot vector Θ_i. Care should be taken in order to avoid collapsing collocation points, which would result in matrices with identical lines being produced.

6. Desingularization of the boundary integral equations

If we consider the interior problem defined in Equation (33), which we denote here for convenience after dropping the *int* superscript,

$$c\boldsymbol{u} + \boldsymbol{\mathcal{N}}\boldsymbol{u} = \boldsymbol{\mathcal{D}}\boldsymbol{f} \qquad \text{in } H^{\frac{1}{2}}(\Gamma), \tag{52}$$

we observe that the operators $\boldsymbol{\mathcal{N}}$ and $\boldsymbol{\mathcal{D}}$ are defined through a Cauchy principal value integral, and a weakly singular integral, which arise from using Green's theorem and the fundamental solutions to formulate the boundary integrals.

12

In three dimensions these are integrals that contain a $(1/r)$ or stronger singularity around the source points. Numerical integration of such singularities is a delicate and ill-conditioned problem, which requires a careful treatment (see, for example, [23] or [45] for an overview of the available techniques).

In [30, 32] it was shown how these singularities can be safely considered artifacts of the convolution with the fundamental solutions. They are not essential to boundary integral formulations, because they can be removed by exploiting the fundamental identities coming from the physical interpretation of the problem. The idea behind these techniques stems from the fact that we know the exact solutions to Equation (52) for all pairs $\boldsymbol{u}_R, \boldsymbol{f}_R$ which represent pure translations and rotations, and clever choices of these solutions can be superimposed on the unknown pair $\boldsymbol{u}, \boldsymbol{f}$ to remove the singularities of both kernels.

In [27, 26, 43] this idea was implemented in a standard BEM code, where the authors show that standard quadrature rules can be used in the resulting boundary integral equations, which become nonsingular.

We adapt these techniques to the collocation isogeometric approximation of three dimensional boundary integral equations for Stokes flow, taking into account the non interpolatory nature of the isogeometric basis, and compare our results with analytical results for simple geometries.

Given a solution $\boldsymbol{u}$ and $\boldsymbol{f}$ of the interior problem (52), and a point $\boldsymbol{y}$ on a smooth portion of Γ, if $\boldsymbol{u}$ and $\boldsymbol{f}$ are continuous on $\boldsymbol{y}$, we can consider the linear velocity

$$\boldsymbol{w}(\boldsymbol{x}; \boldsymbol{u}, \boldsymbol{f}, \boldsymbol{y}) := \boldsymbol{u}(\boldsymbol{y}) + Q(\boldsymbol{f}(\boldsymbol{y}), \boldsymbol{n}(\boldsymbol{y}))(\boldsymbol{x} - \boldsymbol{y}), \tag{53}$$

where the (constant) matrix $Q(\boldsymbol{f}, \boldsymbol{n})$ is defined as

$$Q(\boldsymbol{f}, \boldsymbol{n}) := \boldsymbol{f} \otimes \boldsymbol{n} - \frac{1}{4}(\boldsymbol{f} \cdot \boldsymbol{n})(\boldsymbol{I} + \boldsymbol{n} \otimes \boldsymbol{n}). \tag{54}$$

The divergence of $\boldsymbol{w}$ vanishes everywhere, the pressure is identically zero, and we can express the associated normal stress $\boldsymbol{g}$ as

$$\boldsymbol{g}(\boldsymbol{x}; \boldsymbol{u}, \boldsymbol{f}, \boldsymbol{y}) := \eta\big(Q(\boldsymbol{f}(\boldsymbol{y}), \boldsymbol{n}(\boldsymbol{y})) + Q(\boldsymbol{f}(\boldsymbol{y}), \boldsymbol{n}(\boldsymbol{y}))^T\big)\boldsymbol{n}(\boldsymbol{x}). \tag{55}$$

For any point $\boldsymbol{y}$ on a smooth portion of the boundary, the pair $\boldsymbol{w}$ and $\boldsymbol{g}$ satisfies the boundary integral equation (52), and it is such that the values of $\boldsymbol{w}$ and $\boldsymbol{g}$ computed in $\boldsymbol{x} = \boldsymbol{y}$ are equal to $\boldsymbol{u}(\boldsymbol{y})$ and $\boldsymbol{f}(\boldsymbol{y})$. In particular we have (see the Appendix in [27] for the details of the proof):

$$\begin{aligned} \lim_{\boldsymbol{x} \to \boldsymbol{y}} \big(\boldsymbol{w}(\boldsymbol{x}; \boldsymbol{u}, \boldsymbol{f}, \boldsymbol{y}) - \boldsymbol{u}(\boldsymbol{y})\big) &= O(|\boldsymbol{x} - \boldsymbol{y}|^2) \\ \lim_{\boldsymbol{x} \to \boldsymbol{y}} \big(\boldsymbol{g}(\boldsymbol{x}; \boldsymbol{u}, \boldsymbol{f}, \boldsymbol{y}) - \boldsymbol{f}(\boldsymbol{y})\big) &= O(|\boldsymbol{x} - \boldsymbol{y}|), \end{aligned} \tag{56}$$

which is exactly what is needed to cancel the singularities of the operators $\mathcal{N}$ and $\mathcal{D}$ when evaluated at the point $\boldsymbol{y}$ in Equation (52).

If we repeat this construction for each collocation point $\boldsymbol{x}^\alpha$, and define

$$\begin{aligned} \boldsymbol{w}^\alpha(\boldsymbol{x}) &:= \boldsymbol{w}(\boldsymbol{x}; \boldsymbol{u}, \boldsymbol{f}, \boldsymbol{x}^\alpha) \\ \boldsymbol{g}^\alpha(\boldsymbol{x}) &:= \boldsymbol{g}(\boldsymbol{x}; \boldsymbol{u}, \boldsymbol{f}, \boldsymbol{x}^\alpha) \end{aligned} \tag{57}$$

13

we can subtract from the boundary integral equation for $\boldsymbol{u}$ and $\boldsymbol{f}$ evaluated at the collocation points $\boldsymbol{x}^\alpha$ the corresponding boundary integral equation for $\boldsymbol{w}^\alpha(\boldsymbol{x})$ and $\boldsymbol{g}^\alpha(\boldsymbol{x})$, to obtain a non-singular formulation of the boundary integral equation (thanks to properties (56)) given by

$$\boldsymbol{\mathcal{N}}(\boldsymbol{u} - \boldsymbol{w}^\alpha) = \boldsymbol{\mathcal{D}}(\boldsymbol{f} - \boldsymbol{g}^\alpha) \qquad \text{in } H^{\frac{1}{2}}(\Gamma), \tag{58}$$

where the term $c(\boldsymbol{u}(\boldsymbol{x}^\alpha) - \boldsymbol{w}^\alpha(\boldsymbol{x_\alpha}))$ vanishes, because the two velocities coincide in $\boldsymbol{x}^\alpha$. If we evaluate the boundary integral equation (58) at the collocation point $\boldsymbol{x}^\alpha$, then the singularities in the integrals which define $\boldsymbol{\mathcal{N}}$ and $\boldsymbol{\mathcal{D}}$ are compensated by $(\boldsymbol{u}(\boldsymbol{x}) - \boldsymbol{w}^\alpha(\boldsymbol{x}))$ and $(\boldsymbol{f}(\boldsymbol{x}) - \boldsymbol{g}^\alpha(\boldsymbol{x}))$ which go to zero when $\boldsymbol{x} \to \boldsymbol{x}^\alpha$ with the right powers, leaving us with a formulation which does not require any singular integration.

In Equation (58), the functions $\boldsymbol{w}^\alpha$ and $\boldsymbol{g}^\alpha$ depend linearly on the solution $\boldsymbol{u}, \boldsymbol{f}$. In particular we can define the following three operators:

$$\begin{aligned}
\boldsymbol{\mathcal{M}}(\boldsymbol{y}) :& C^0(B_\varepsilon(\boldsymbol{y}) \cap \Gamma) \mapsto \Re^d \\
& \big(\boldsymbol{\mathcal{M}}(\boldsymbol{y})\boldsymbol{u}\big)(\boldsymbol{x}) = \boldsymbol{u}(\boldsymbol{y}) \\
\boldsymbol{\mathcal{W}}(\boldsymbol{y}) :& C^0(B_\varepsilon(\boldsymbol{y}) \cap \Gamma) \mapsto H^{\frac{1}{2}}(\Gamma) \\
& \big(\boldsymbol{\mathcal{W}}(\boldsymbol{y})\boldsymbol{f}\big)(\boldsymbol{x}) = Q(\boldsymbol{x}; \boldsymbol{f}(\boldsymbol{y}), \boldsymbol{n}(\boldsymbol{y}))(\boldsymbol{x} - \boldsymbol{y}) \\
\boldsymbol{\mathcal{G}}(\boldsymbol{y}) :& C^0(B_\varepsilon(\boldsymbol{y}) \cap \Gamma) \mapsto H^{-\frac{1}{2}}(\Gamma) \\
& \big(\boldsymbol{\mathcal{G}}(\boldsymbol{y})\boldsymbol{f}\big)(\boldsymbol{x}) = \eta\big(Q(\boldsymbol{x}; \boldsymbol{f}(\boldsymbol{y}), \boldsymbol{n}(\boldsymbol{y})) + Q(\boldsymbol{x}; \boldsymbol{f}(\boldsymbol{y}), \boldsymbol{n}(\boldsymbol{y}))^T\big)
\end{aligned} \tag{59}$$

where $B_\varepsilon(\boldsymbol{y})$ is the ball of radius ε centered in $\boldsymbol{y}$, and ε is arbitrarily small, such that its intersection with Γ remains smooth.[3] Using these operators we can rewrite $\boldsymbol{w}$ and $\boldsymbol{g}$ as

$$\begin{aligned}
\boldsymbol{w}^\alpha &= \boldsymbol{\mathcal{M}}(\boldsymbol{x}^\alpha)\boldsymbol{u} + \boldsymbol{\mathcal{W}}(\boldsymbol{x}^\alpha)\boldsymbol{f} \\
\boldsymbol{g}^\alpha &= \boldsymbol{\mathcal{G}}(\boldsymbol{x}^\alpha)\boldsymbol{f}.
\end{aligned} \tag{60}$$

If we leave the term of $\boldsymbol{w}^\alpha$ that depends on $\boldsymbol{u}$ on the left hand side in Eq. (58), and move the term that depends on $\boldsymbol{f}$ on the right hand side, we obtain

$$\boldsymbol{\mathcal{N}}(\boldsymbol{u} - \boldsymbol{u}(\boldsymbol{x}^\alpha)) = \boldsymbol{\mathcal{D}}(\boldsymbol{f} - \boldsymbol{g}^\alpha) + \boldsymbol{\mathcal{N}}Q^\alpha(\boldsymbol{x} - \boldsymbol{x}^\alpha) \qquad \text{in } H^{\frac{1}{2}}(\Gamma), \tag{61}$$

which can be rewritten using the operators in Equation (60) as

$$\boldsymbol{\mathcal{N}}\big(\boldsymbol{I} - \boldsymbol{\mathcal{M}}(\boldsymbol{x}^\alpha)\big)\boldsymbol{u} = \Big(\boldsymbol{\mathcal{D}}\big(\boldsymbol{I} - \boldsymbol{\mathcal{G}}(\boldsymbol{x}^\alpha)\big) + \boldsymbol{\mathcal{N}}\boldsymbol{\mathcal{W}}(\boldsymbol{x}^\alpha)\Big)\boldsymbol{f} \qquad \text{in } H^{\frac{1}{2}}(\Gamma). \tag{62}$$

If we discretize directly Equation (62) instead of Equation (52), we obtain a non-singular formulation of the boundary integral equations that can be expressed in the form

$$\boldsymbol{H}\boldsymbol{u} = \boldsymbol{L}\boldsymbol{f}, \tag{63}$$

---

[3]This assumption implies, in particular, that collocation points should not be positioned on corners, since in that case the normal would not be uniquely defined, and the present technique would not be applicable.

14

where the entries of the matrices $\boldsymbol{H}$ and $\boldsymbol{L}$ are given by

$$\boldsymbol{H}^{(d\alpha+a)(j)} = \boldsymbol{e}_a \cdot \big(\boldsymbol{\mathcal{N}}(\boldsymbol{I} - \boldsymbol{\mathcal{M}}(\boldsymbol{x}^\alpha))\boldsymbol{\tau}^j\big)(\boldsymbol{x}^\alpha)$$
$$\boldsymbol{L}^{(d\alpha+a)(j)} = \boldsymbol{e}_a \cdot \Big(\big(\boldsymbol{\mathcal{D}}(\boldsymbol{I} - \boldsymbol{\mathcal{G}}(\boldsymbol{x}^\alpha)) + \boldsymbol{\mathcal{N}}\boldsymbol{\mathcal{W}}(\boldsymbol{x}^\alpha)\big)\boldsymbol{\tau}^j\Big)(\boldsymbol{x}^\alpha). \tag{64}$$

In the definition (64), we observe that all operators are linear, and allow us to rewrite the system as

$$\boldsymbol{H}\boldsymbol{u} := (\boldsymbol{N} + C\boldsymbol{M})\boldsymbol{u} = (\boldsymbol{D} + B\boldsymbol{M})\boldsymbol{f} =: \boldsymbol{L}\boldsymbol{f}, \tag{65}$$

where the matrices $\boldsymbol{H}$ and $\boldsymbol{L}$ can be constructed *a posteriori* with elementary linear algebra operations starting from the matrices $\boldsymbol{M}$, $\boldsymbol{N}$ and $\boldsymbol{D}$ defined in Equations (47–49), where the integrations are computed using standard quadrature formulas, ignoring the inaccuracies that will be accumulated around the diagonals of $\boldsymbol{N}$ and $\boldsymbol{D}$.

In particular, we have

$$(C\boldsymbol{M})^{(d\alpha+a)(j)} = \boldsymbol{e}_a \cdot \big(-\boldsymbol{\mathcal{N}}\boldsymbol{\mathcal{M}}(\boldsymbol{x}^\alpha)\boldsymbol{\tau}^j\big)(\boldsymbol{x}^\alpha)$$
$$(B\boldsymbol{M})^{(d\alpha+a)(j)} = \boldsymbol{e}_a \cdot \Big(\big(-\boldsymbol{\mathcal{D}}\boldsymbol{\mathcal{G}}(\boldsymbol{x}^\alpha) + \boldsymbol{\mathcal{N}}\boldsymbol{\mathcal{W}}(\boldsymbol{x}^\alpha)\big)\boldsymbol{\tau}^j\Big)(\boldsymbol{x}^\alpha), \tag{66}$$

where the matrix C is diagonal and the matrix B is composed of n blocks of dimension $d \times d$ on the diagonal.

In a way that is very similar to the rigid body mode or rigid mode technique [16], we exploit the fact that, by construction, the final system has to solve exactly the dn pairs of solutions $\boldsymbol{w}^\alpha$ and $\boldsymbol{g}^\alpha$ associated with the basis functions of V_h.

For a given basis function $\boldsymbol{\tau}^i$, its associated pair $\boldsymbol{w}^\alpha$ and $\boldsymbol{g}^\alpha$ will be different from zero only if $\boldsymbol{x}^\alpha$ belongs to its support, therefore the only entries of the matrices $\boldsymbol{D}$ and $\boldsymbol{N}$ that will be corrected are those around the diagonal. Explicit calculations of B and C will be given below.

This process is easily implemented when the finite dimensional space is of Lagrangian type, i.e., when $\phi^\beta(\boldsymbol{x}^\alpha) = \delta_{\beta\alpha}$. In this case the singular diagonal blocks of the matrices $\boldsymbol{N}$ and $\boldsymbol{D}$ can be expressed in terms of the remaining parts of the same matrices, exploiting the formulation (58), as shown in [43].

In the isogeometric case, however, the basis functions are not of interpolatory type, and the *a posteriori* implementation requires a little more attention, hence the corrections in the forms $C\boldsymbol{M}$ and $B\boldsymbol{M}$. Notice that on the left hand side we obtain the same kind of indirect regularization that was used in Equation (50).

In order to compute the B matrix, we start with the consideration that the value of the a-th coefficient of the NURBS function $\boldsymbol{u}(\boldsymbol{x})$ in the point $\boldsymbol{x}^\alpha$ is obtained by reading the $d\alpha + a$ column of the matrix-vector multiplication between $\boldsymbol{M}$ and the vector $\boldsymbol{u}$ of coefficients defining $\boldsymbol{u}(\boldsymbol{x})$:

$$(\boldsymbol{M}\boldsymbol{u})^{(d\alpha+a)} = u_a(\boldsymbol{x}^\alpha). \tag{67}$$

In the case of Lagrange finite dimensional spaces, the collocation matrix $\boldsymbol{M}$ is the identity matrix, and the procedure outlined in [43] can be applied directly. For an isogeometric collocation boundary element discretization, the matrices $\boldsymbol{N}$, $\boldsymbol{D}$ and $\boldsymbol{M}$ should be multiplied with vectors of *coefficients*, not nodal values. We exploit the well known property of NURBS functions, by which interpolation of the control polygon

15

commutes with affine transformations to express the coefficients defining the dn pairs of functions $\boldsymbol{w}^\alpha$ and $\boldsymbol{g}^\alpha$ as

$$
\begin{aligned}
\boldsymbol{W}^{(d\beta+a)(d\alpha+b)} &= \sum_{c=0}^{d-1} Q_{ac}^{b,\alpha}(\boldsymbol{c}^{d\beta+c} - \boldsymbol{x}_c^\alpha) \\
\boldsymbol{G}^{(d\beta+a)(d\alpha+b)} &= \sum_{c=0}^{d-1} \eta(Q_{ac}^{b,\alpha} + Q_{ca}^{b,\alpha})\bar{\boldsymbol{n}}^{d\beta+c},
\end{aligned}
\tag{68}
$$

where $\bar{\boldsymbol{n}}$ is the L^2 projection of the normal in the NURBS space, $\boldsymbol{c}$ is the control polygon that defines the geometry, $\boldsymbol{\tau}$ are the basis functions of V_h and the matrices $Q^{a,\alpha}$ are given by

$$
Q^{a,\alpha} := \boldsymbol{e}_a \otimes \boldsymbol{n}(\boldsymbol{x}^\alpha) - \frac{1}{4}n_a(\boldsymbol{x}^\alpha)\big(\boldsymbol{I} + \boldsymbol{n}(\boldsymbol{x}^\alpha) \otimes \boldsymbol{n}(\boldsymbol{x}^\alpha)\big).
\tag{69}
$$

The isogeometric regularization of the matrices $\boldsymbol{N}$ and $\boldsymbol{D}$ through the matrices C and B can then be computed as

$$
\begin{aligned}
C^{ij} &:= -\delta_{ij} \sum_{k=0}^{dn-1} \boldsymbol{N}^{ik} \\
B^{(d\alpha+i)(d\alpha+j)} &= \sum_{a=0}^{dn-1} \Big(-\boldsymbol{D}^{(d\alpha+i)(a)}\boldsymbol{G}^{(a)(d\alpha+j)} + \boldsymbol{N}^{(d\alpha+i)(a)}\boldsymbol{W}^{(a)(d\alpha+j)}\Big).
\end{aligned}
\tag{70}
$$

The correction applied to the system by the matrices C and B takes into account the knowledge of the exact solutions $\boldsymbol{w}^\alpha$ and $\boldsymbol{g}^\alpha$ in the point $\boldsymbol{x}^\alpha$ to correct the singular entries in $\boldsymbol{N}$ and $\boldsymbol{D}$, similarly in spirit to what is done in the rigid body technique.

For this technique to be accurate and efficient, quadrature formulas that guarantee an accurate integration of the non singular portion of Γ should be used.

7. Numerical Verification

One of the advantages of using NURBS basis functions for the geometry description, is the possibility to represent exactly conic curves. In this section we compare several numerical experiments with known analytical results for spheroids in uniform flows, using both standard integrations (based on the works by Lachat and Watson [28] and by Telles [45]) as well as the techniques exposed in Section 6.

A prolate spheroid of eccentricity $e := \sqrt{1 - (a/b)^2}$ is defined as the surface of revolution around the z axis of an ellipse with semi-minor and semi-major axes a and b, implicitly defined by the equation

$$
\frac{x^2 + y^2}{a^2} + \frac{z^2}{b^2} = 1, \qquad a \le b.
\tag{71}
$$

We indicate with λ the ratio $b/a \ge 1$, and we fix the volume of the spheroid to be equal to that of a sphere with unit radius, corresponding to the choice $\lambda = 1$, $a = b = 1$.

In [7] it is argued that Gaussian quadrature rules may not be efficient in isogeometric analysis, since they do not exploit the interelement regularity which is typical of B-Splines

16

and NURBS. Efficient rules are devised in [7] for the integration of mass and stiffness matrices in isogeometric analysis.

In the case of boundary integral operators, however, the integrands contain non linear terms depending on different powers of the distance between the quadrature point and the evaluation point, and the quadrature rules which have been devised there might not be optimal in this case.

In our first set of experiments, we show how in non-singular boundary integral equations, i.e., where the singularity is far away from the integration surface, in some cases standard Gaussian quadrature rules fail to deliver a convergence rate which is independent on the geometry. On surfaces with high curvatures this is even more evident than in standard IGA analysis, and the authors are currently working on devising alternative quadrature methods that will provide optimal convergence results for standard integrals independently on the curvature.

This consideration is common to all IGA-BEM methods, not only to the one presented in this paper, since Gauss quadrature rules are still the de-facto standard integration tool for boundary element methods in all cases where the singularity is far away from the singularity.

When implementing a boundary element approximation, the following crucial points should be taken in consideration, both in standard BEM as well as in IGA-BEM:

1. An efficient and accurate integration method should be used, capable of integrating to a good degree of accuracy polynomial or rational functions on curved geometries, weighted with $(1/r)$ or $(1/r)^2$, when $r > 0$;
2. A strategy should be chosen to integrate in regions which contain a singularity of type $(1/r)$ or $(1/r^2)$, such as the one presented in this paper, or one based on special quadrature techniques, such as those presented in [45] or [28], or any other technique to approximate Cauchy Principal value integrals (see, for example, [23]).

In the tests that follow, we asses the quality of standard Gaussian quadrature rules to address Point 1 in Section 7.1, and we show some critical points which have to be taken under consideration also when using isogeometric approximations. In Section 7.2 we make some considerations on the approximation capabilities of the iso-geometric space V_h when it comes to approximating the normal vector field, discussing some of the consequences on the convergence of numerical methods. We compare the computational cost between the technique introduced in Section 6 and standard singular integration techniques in Section 7.3, while Point 2 above is explored in detail in Section 7.4, where we asses the accuracy of the method introduced in this paper and we compare it to other integration methods introduced in [28] and in [45].

The validation and the test cases we present here were implemented in Matlab [33], using the NURBS toolbox [41]. Similar functionalities, which are tailored mostly for FE-IGA applications, are available in the `GeoPDEs` package [18], an open source library for isogeometric analysis.

7.1. Geometry discretization and quadrature rules for non singular integration

The nonsingular integration method we presented in Section 6 hinges upon the assumption that it is possible to integrate effectively and accurately the non singular parts of the boundary integral equations.
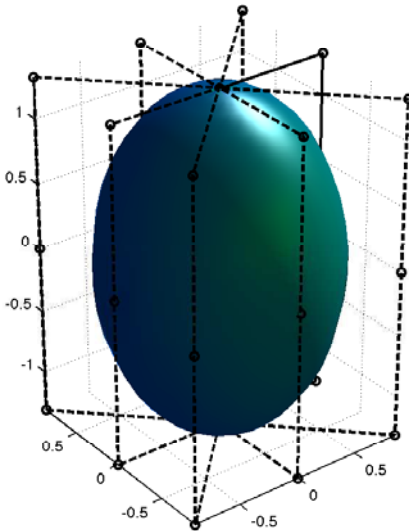
17

Figure 1: Control net and NURBS surface of a prolate spheroid with ratio $\lambda = 1.5$.

In this section we present a set of tests on simple geometries with different curvatures aimed at selecting reasonable quadrature rules for the integration of the non singular parts of the boundary integral equations, which are crucial for the accuracy of the non-singular method presented in Section 6, and we quantify the influence of the geometry on the integration strategies.

We construct our prolate spheroids starting from a circular arc which is deformed to an ellipse and revolved around the z axis. Figure 1 shows an example of the coarsest control net used for our simulations, for the case $\lambda = 1.5$. An exact representation of these conic curves can be obtained with quadratic NURBS for both the z-direction, and the revolution direction. In the z-direction the knot span used to generate the surface of revolution is given by $\{0, 0, 0, 1/2, 1/2, 1, 1, 1\}$, with control points and weights given in Table 1.

	c^0	c^1	c^2	c^3	c^4
x	0.0000	0.6177	0.8736	0.6177	0.0000
y	0	0	0	0	0
z	-1.3104	-0.9266	0	0.9266	1.3104
w	1.0000	0.7071	1.0000	0.7071	1.0000

Table 1: Control points for half ellipse with $\lambda = 1.5$. Last line contains the weights of the NURBS basis.

The revolution around the z-axis generates a NURBS surface with 45 control points

18

(5 in the z-direction, and 9 in the revolution direction). The knot spans have respectively 3 and 5 non zero segments, which are split at the abscissae of the collocation points, and then filled with Gauss quadrature points.

Whenever the evaluation point for the boundary integral representation given in Equations (28) and (29) is not on the boundary Γ of the domain Ω, then the integrands defined in Equations (30) and (31) are regular, and their integration is possible with standard quadrature rules.

We construct quadrature rules based on tensor product repetitions of standard Gaussian quadrature rules on each non-zero interval of the union between the knot spans and the abscissas of the collocation points. This choice is driven by the consideration that, while the desingularization technique introduced in Section 6 produces integrands which are non singular, in general they are only continuous at the collocation points. Although Gauss quadrature rules converge also for functions which are only continuous, their convergence speed would suffer from the limited regularity. On the other hand, splitting the elements at collocation abscissae removes these limitations and allows us to use standard Gauss quadrature rules with the nonsingular technique introduced in Section 6 in a very effective way.

In order to select a sufficiently accurate quadrature rules for non-singular integrals, we test some boundary integral identities on different prolate spheroids, with λ ranging from one to two, where the singularity is placed inside or outside of the domain. For comparison purposes only, we also test these identities in the singular case, i.e., when the evaluation point lyes on the boundary itself. In this case we expect standard quadrature rules not to converge, and we show in these examples how they actually fail.

We measure the norms of $E^i(\boldsymbol{x})$, defined as

$$E_a^0(\boldsymbol{x}) := \frac{1}{8\pi} \int_\Gamma \mathcal{S}_{ab}(\boldsymbol{x} - \boldsymbol{y}) n_b(\boldsymbol{y}) \, \mathrm{d}\Gamma(\boldsymbol{y}) \qquad\qquad = 0 \quad \forall \boldsymbol{x} \in \Re^d \tag{72}$$

$$E_{ab}^1(\boldsymbol{x}) := \frac{1}{8\pi} \int_\Gamma \mathcal{T}_{abc}(\boldsymbol{x} - \boldsymbol{y}) n_c(\boldsymbol{y}) \, \mathrm{d}\Gamma(\boldsymbol{y}) \qquad\qquad = 0 \quad \forall \boldsymbol{x} \in \Re^d \setminus \overline{\Omega} \tag{73}$$

$$E_{ab}^2(\boldsymbol{x}) := \frac{1}{8\pi} \int_\Gamma \mathcal{T}_{abc}(\boldsymbol{x} - \boldsymbol{y}) n_c(\boldsymbol{y}) \, \mathrm{d}\Gamma(\boldsymbol{y}) - \delta_{ab} \qquad = 0 \quad \forall \boldsymbol{x} \in \Omega \tag{74}$$

$$E_{ab}^3(\boldsymbol{x}) := \frac{1}{8\pi} \int_\Gamma \mathcal{T}_{abc}(\boldsymbol{x} - \boldsymbol{y}) n_c(\boldsymbol{y}) \, \mathrm{d}\Gamma(\boldsymbol{y}) - \frac{1}{2}\delta_{ab} \qquad = 0 \quad \forall \boldsymbol{x} \in \Gamma, \tag{75}$$

in three points, respectively $\boldsymbol{x}^0 = (1, 2, 3)^T \in \Re^d \setminus \overline{\Omega}$, $\boldsymbol{x}^1 = (.1, .3, .2)^T \in \Omega$ and $\boldsymbol{x}^2 = (a, 0, 0)^T \in \Gamma$, using different number of quadrature points in each interval.

The results are summarised in Figures 2, 3 and 4. A close inspection reveals that the computed quantities in the exterior part of the domain (i.e., for $\boldsymbol{x} = \boldsymbol{x}^0$) converge at the same rate almost independently of the spheroid geometry.

In the interior case (i.e., when $\boldsymbol{x} = \boldsymbol{x}^1$) the geometry seems to play a more important role, and the convergence rates deteriorate when the curvature is higher, even though we observe a uniform behaviour with respect to the number of quadrature points in each fixed geometry.

In the singular case (i.e., when $\boldsymbol{x} = \boldsymbol{x}^2$) the deterioration of the accuracy of the integrals is expected and it is the main reason for devising alternative integration techniques, such as, for example, those presented in [45] or [28], or the ones introduced in Section 6.
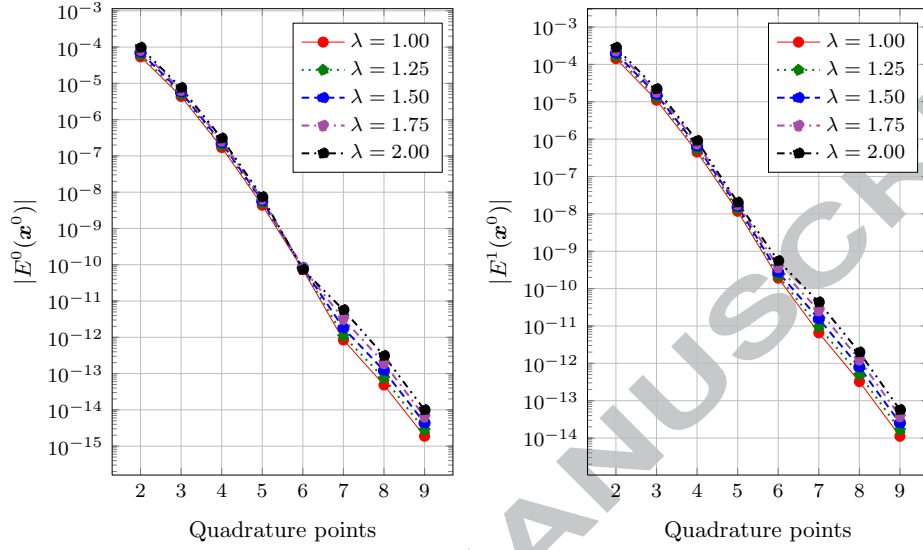
19

Figure 2: Norm of $E^0(\boldsymbol{x}^0)$ (left) and $E^1(\boldsymbol{x}^0)$ for different numbers of quadrature points.
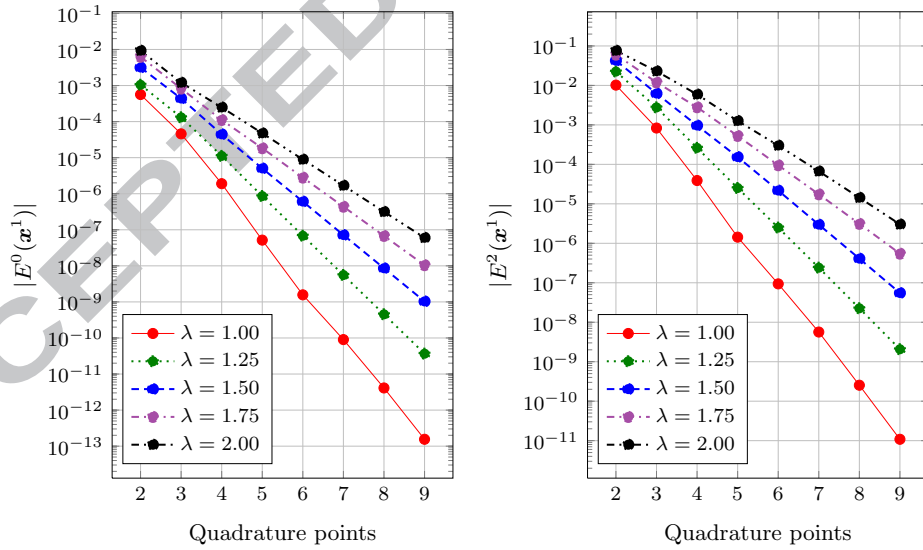

Figure 3: Norm of $E^0(\boldsymbol{x}^1)$ (left) and $E^2(\boldsymbol{x}^1)$ for different numbers of quadrature points.
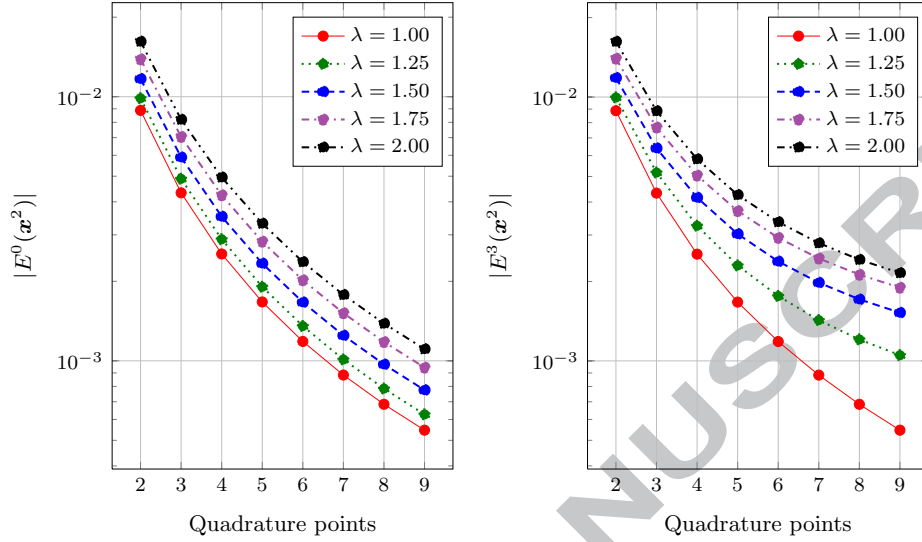
20

Figure 4: Norm of $E^0(\boldsymbol{x}^2)$ (left) and $E^3(\boldsymbol{x}^2)$ for different numbers of quadrature points.

Somewhat surprising are the results which emerge from Figure 3, since they show a quite drastic dependency on the geometry of standard Gauss quadrature rules when applied to non-singular boundary integrals. This problem is present also in standard IGA analysis, but it seems more important in boundary integral equations, probably due to the presence of the $1/r^p$ terms in the integrands. In IGA analysis, Gauss quadrature rules are sub-optimal, as is shown, for example, in [7]. This is not to say that they do not converge to the correct solution (as Figure 2 and 3 show) when raising the number of quadrature points, but simply that some care should be taken when high order quadrature rules are required (for example when performing p-refinements), since merely increasing the number of quadrature points may not the best strategy to tackle IGA problems in general.

The results in Figures 2, 3 and 4 are obtained with the coarse knot span produced by the NURBS toolbox. If we fix the number of quadrature points to five and eight and raise the number of control points by k-refinement, i.e., by inserting equally spaced knots in the knot span, for the worst case scenario of $E^2(\boldsymbol{x}^1)$, we obtain the results presented in Figure 5, which shows how also when using relatively cheap Gauss quadrature rules, we can obtain very good convergence properties (up to machine precision) for the non-singular boundary integral identities, even though the underline quadrature formulas are not optimal nor independent on the geometry.

The singular case, shown in Figure 6, is very sensitive with respect to the position of the singularity (which here coincides with the image of a collocation point), and deteriorates very quickly when the singular points get closer and closer to the quadrature points.

A deeper investigation is required, maybe following [7], to exploit the additional interelement regularity of NURBS basis functions in selecting optimal quadrature rules

21
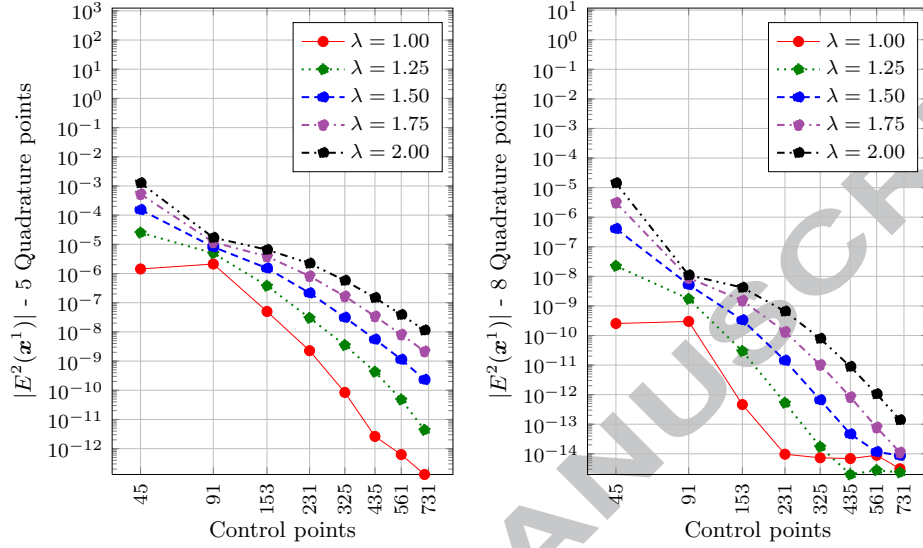
Figure 5: Norm of $E^2(\boldsymbol{x}^1)$ for 5 quadrature points (left) and for 8 quadrature points (right) for different numbers of control points.
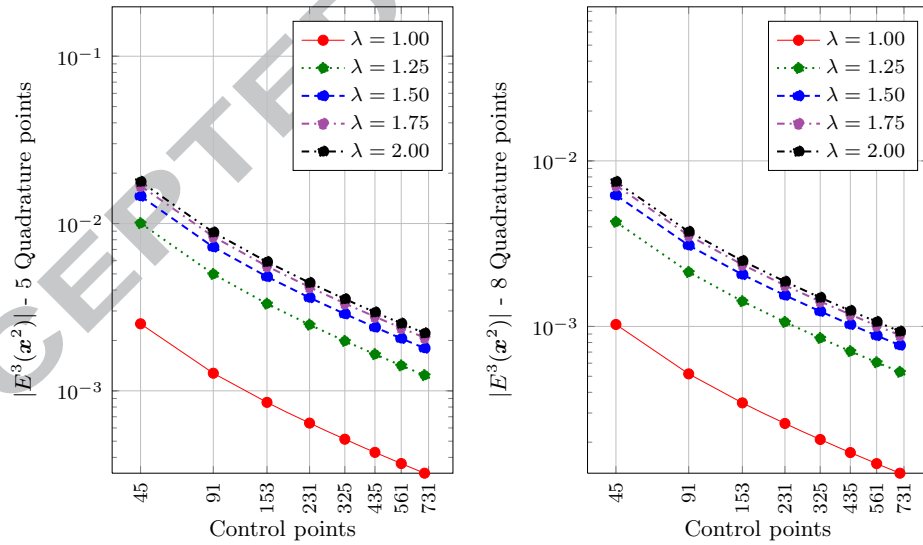

Figure 6: Norm of $E^3(\boldsymbol{x}^2)$ for 5 quadrature points (left) and for 8 quadrature points (right) for different numbers of control points.

22

for nonsingular boundary element method formulations such as the one presented in this paper. Following the results presented in these tests, we fixed the number of quadrature points to six and eight and performed the following tests using k-refinement, for both quadratic and cubic NURBS.

In the authors' experience, raising the number of Gauss quadrature points over eight points per direction does not improve significantly the accuracy of any of the considered methods (at least in the quadratic and cubic cases), while it increases significantly their computational costs. A possible explanation for this behaviour is presented in the next section.

7.2. Representation of the normal vector field

A key and delicate aspect of all boundary integral discretizations is the accurate representation of the normal vector field $\boldsymbol{n}$ in the finite dimensional space V_h.

For iso-geometric spaces defined on non-trivial geometries, the normal vector $\boldsymbol{n}$ does not belong to V_h. While this may seem like a non-issue, it impacts negatively on both the convergence properties of the method, and on the possibility to represent exactly trivial solutions.

Take, for example, a given linear velocity field of the kind

$$\boldsymbol{u}_g = Q(\boldsymbol{x} - \boldsymbol{x}_o), \tag{76}$$

where Q is a constant 3×3 matrix with zero trace and $\boldsymbol{x}_0$ is an arbitrary point. An exact representation of $\boldsymbol{u}$ on Γ is possible in the finite dimensional space V_h because the space is iso-geometric, and therefore it can represent exactly affine transformations of points $\boldsymbol{x}$ on the boundary. The velocity $\boldsymbol{u}_g$ is constructed precisely as an affine transformation of the vector $\boldsymbol{x}$.

In the interior problem, this velocity admits the zero pressure solution

$$\boldsymbol{\sigma}_g = \eta(Q + Q^T), \tag{77}$$

where $\boldsymbol{\sigma}_g$ is the Cauchy stress solution associated to $\boldsymbol{u}_g$, and it is a constant symmetric tensor. Since $\boldsymbol{n}$, in general, does not belong to V_h, the normal stress $\boldsymbol{f}_g := \boldsymbol{\sigma}_g \boldsymbol{n}$ cannot belong to V_h either, since it is an affine transformation of $\boldsymbol{n}$, and therefore it is not possible to represent *exactly* the solution to $\boldsymbol{u}_g$.

A general consequence of this lack of representability of the normal $\boldsymbol{n}$ is that the L^2 error of the solution will in general be dominated by the error in the approximation of the normal $\boldsymbol{n}$ (an error which is purely *geometric*), that is:

$$\|\boldsymbol{f}_h - \boldsymbol{f}_{exact}\| \sim \|\boldsymbol{n}_h - \boldsymbol{n}_{exact}\|, \tag{78}$$

independently on the technique that was used to compute the singular integrals.

To give a sense of what is the influence of this error, we report in Figure 7 the error in the representation of the normal, when $\boldsymbol{n}_h$ is computed as the L^2 projection of $\boldsymbol{n}$, for the geometries that were introduced in the previous section. The geometry where $\lambda = 1.00$ has not been plotted, since that is the only case in which the normal is *exact*, and the error remains at the machine level for all numbers of control points.

Independently on the accuracy of the integration techniques, the L^2 error between the computed solution and the exact solution (in which also the normal is computed
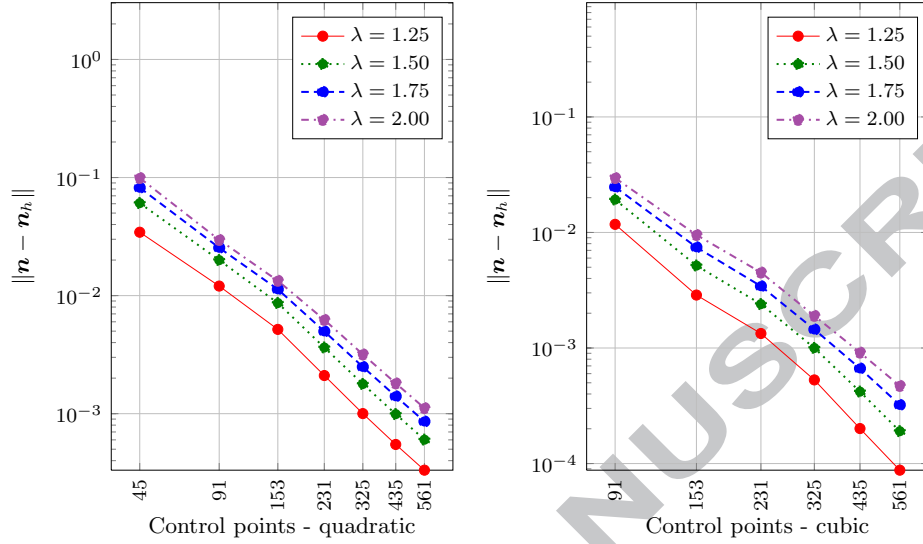
23

Figure 7: L^2 error in the representation of the normal $\boldsymbol{n}$ for different number of control points, with quadratic NURBS (left) and with cubic NURBS (right), based on standard 8 points Gauss quadrature rules. Increasing the number of quadrature ponts does not improve the graph any further.

exactly) will be bounded by the values in Figure 7. For the range of numbers of degrees of freedom we have chosen, the minimum of these values go between 10^{-3} for quadratic NURBS and 10^{-4} for cubic NURBS, with significant differences between large curvature geometries ($\lambda \sim 2.00$) and small curvature ones ($\lambda \sim 1$).

7.3. Cost comparison with standard singular-quadrature techniques

In this section we compare the computational cost of the desingularization technique presented in Section 6 when compared to two classical integration methods. The first one is based on the work by Lachat and Watson [28], while the second exploits Telles transformations [45]. Both methods are based on singularity removal by local change of variables.

The principle behind these classical integration techniques is that every collocation point can be isolated into well separated square boxes, where it occupies the position $\bar{\xi}$. An appropriate change of variables can then be introduced, such that

$$
\begin{aligned}
B := [0,1]^d, \qquad & \eta : B \mapsto B, \qquad J := \frac{\partial \eta}{\partial \xi} \\
\eta(\partial B) \equiv \partial B, \qquad & \det J > 0 \quad \forall \xi \neq \bar{\xi}, \qquad \det J|_{\bar{\xi}} = 0.
\end{aligned}
\tag{79}
$$

When using this transformation combined with appropriate integration formulas for the evaluation of singular integrals, the zeroth Jacobian compensates for the singularity of the kernels.

In the method proposed by Lachat and Watson in [28], each box B is split into triangles which have one vertex in $\bar{\xi}$. At the edges of the domain the collocation point

24

$\bar{\xi}$ may be on a vertex or on a edge, in which cases two or three triangles are enough. In general four triangles are needed around each collocation point.

A standard quadrature formula on the reference square is chosen and mapped to each of the triangles, by collapsing two vertices of the square on the vertex coinciding with $\bar{\xi}$. The final quadrature formula is obtained by glueing together all the patches, it preserves the accuracy of the original one, and has the characteristic that its Jacobian is zero at $\bar{\xi}$.
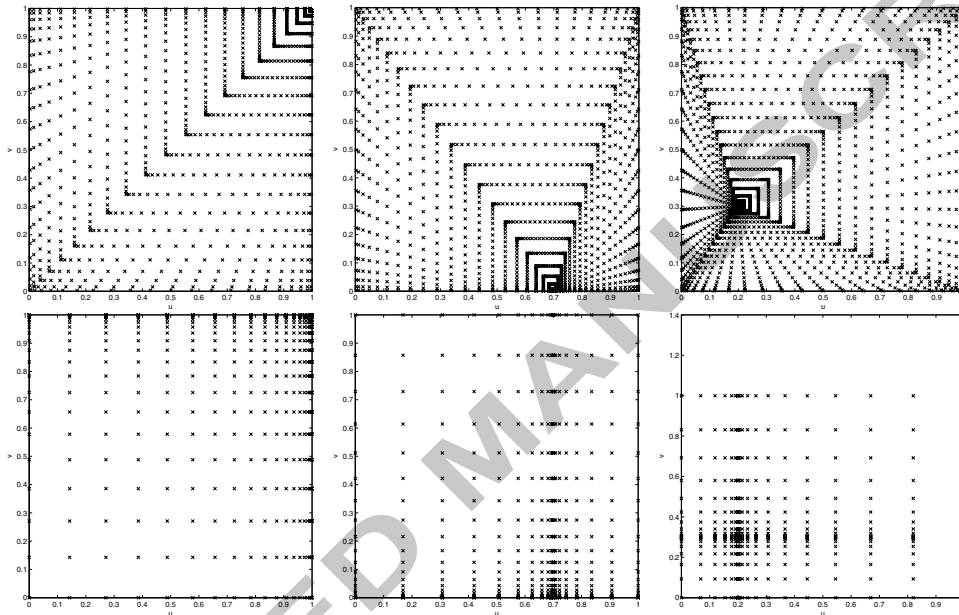
Figure 8: Singular quadrature formulas based on Lachat-Watson (top) and Telles transformations (bottom) for singularities on the points $(1,1)$ (left), $(.7, 0)$ (center), and $(.2, .3)$ (right), based on equi-spaced quadrature rules with 21×21 points.

A similar procedure is presented by Telles in [45], but there the transformation is obtained by tensor product from one dimensional quadratic or cubic transformations which have zero derivatives in $\bar{\xi}$. The resulting quadrature formulas are cheaper to evaluate with respect to the Lachat-Watson ones, and when they are based on cubic transformations they can also have zero second order derivatives at $\bar{\xi}$, which contributes in improving their effectiveness in singular integrations.

Examples of such constructions are outlined in Figure 8, where we pick three possible locations of the singularities, and we construct both a simple Lachat-Watson quadrature formula and a Telles quadrature formula starting from the tensor product of a 21 equi-spaced points quadrature rules (only for illustrational purposes in the Figures).

By construction, the Lachat-Watson technique is well suited for weakly singular integrals, and its effectiveness is usually increased by raising the number of quadrature points in the angle direction, or by combining it with a Telles transformation along the radial direction, which would allow to have also second order derivatives at $\bar{\xi}$ equal to zero.

25

Moreover, in the Lachat-Watson case the singularity is constrained to be inside the reference square, while in the Telles quadrature it can be at arbitrary locations, which makes it also usable for quasi-singular integrals, i.e., for those integrals in which the singularity is close to, but outside, the panel where the integration is occurring. In the examples depicted in Figure 8, the quadrature rules based on Telles transformation are respectively two, three and four times cheaper than the Lachat-Watson ones.
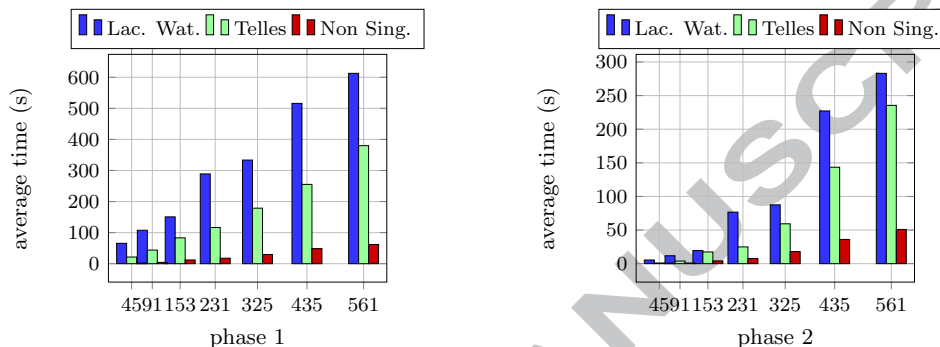

Figure 9: Average cost between standard IGA-BEM and non-singular IGA-BEM for 8 quadrature points.

In Figure 9 we present a comparison of the cost associated to the various phases of the numerical integration procedure using Lachat-Watson integration, Telles integration and non-singular integration. These phases can be summarised as follows

phase 1: Pre-caching of all basis function values and gradients in each of the quadrature points and in each of the collocation points;

phase 2: Integration of the boundary integral equations into system matrices;

phase 3: Linear system solution.

Only phase one and phase two are plotted, since there are no significant differences in phase 3 (the linear system is of the same size in all cases). All methods have been implemented without any special optimization. In particular, we observe that a much greater effort is required in the evaluation of the basis functions if singular quadrature rules are used, since there have to be a specialisation of the quadrature rule for each panel of integration, resulting in a much higher number of basis function evaluations. The difference in total execution time is in the order of one order of magnitude faster when using standard integration and the desingularization technique introduced in Section 6.

These results are the average of five simulations, on a Intel Xeon quad core machine with 8GB of memory, running Linux operating system, where we maintained the comparisons as fair as possible, i.e., we maintained the number of quadrature points for the generating Gauss quadrature rules equal to eight in all cases, even though it is well-known for the Lachat-Watson regularization technique that more integration points should be chosen in the angle direction than in the radial direction.

26

7.4. Accuracy comparison on translating prolate spheroids

Prolate spheroids are a suitable test case for the validation of boundary integral methods, since their traction is known analytically (see, for example, [13]), and the characteristics of the solution allow one to test the behavior of the numerical scheme for high curvatures near the axis of symmetry as well as away from it, by simply modifying the spheroid eccentricity.

When such an object moves uniformly in a quiescent Stokes flow with constant velocity $\boldsymbol{U} = u_x \boldsymbol{e}_x + u_z \boldsymbol{e}_z$, and no-slip boundary conditions on the surface of the body, the total drag it experiences can be expressed as

$$\boldsymbol{F} = 6\pi\nu b(u_x c_x \boldsymbol{e}_x + u_z c_z \boldsymbol{e}_z), \tag{80}$$

where

$$
\begin{aligned}
c_x &:= \frac{16}{3} e^3 \left(2e + (3e^2 - 1) \ln \frac{1+e}{1-e} \right)^{-1}, \\
c_z &:= \frac{8}{3} e^3 \left(-2e + (1+e^2) \ln \frac{1+e}{1-e} \right)^{-1}.
\end{aligned}
\tag{81}
$$

In this section we show the results for the three different three-dimensional solver, testing both different geometries as well as different angles of translation. In particular we report the error in the drag experienced by the sphere, and by spheroids with ratios ranging from $\lambda = 1$ to $\lambda = 2$, for refinement levels and fixing the number of quadrature points per segment to be equal to eight.

The velocities are selected to be

$$\boldsymbol{U}^i = \cos(\theta^i)\boldsymbol{e}_x + \sin(\theta^i)\boldsymbol{e}_z, \qquad \theta^i := \frac{\pi}{2}\frac{i}{9}, \qquad i = 0, \ldots, 9, \tag{82}$$

and we measure the relative errors in percentage, defined as

$$\boldsymbol{E}_F^i := 100 \frac{|\boldsymbol{F}_h - \boldsymbol{F}(\theta^i)|}{|\boldsymbol{F}(\theta^i)|}. \tag{83}$$

An example solution is presented in Figure 10, where we show in color the magnitude of the velocity field for a prolate spheroid in uniform flow, together with the projection on three orthogonal planes of the streamlines in the case $\theta = \theta^8$, and $\lambda = 1.5$. Detailed error results are presented in Table 2 for $\lambda = 1$, Table 3 for $\lambda = 1.5$ and Table 4 for $\lambda = 2$ when using and quadratic NURBS, and integrating with the non-singular approach.

We observe that, with respect to the results presented in [27] and [43], we obtain much smaller errors in all cases. A summary of the worst case scenario using Lachat Watson integration, Telles integration and the non-singular method is shown in Figures 11, 12 and 13 where the behaviour of the maximum error under k-refinement in the quadratic and cubic cases is shown.

We observe that the results obtained with the Lachat Watson quadrature technique (Figure 11) is very robust in terms of dependency on the geometry, but it is also the one that attains the highest errors, when compared both with the Telles method (Figure 12) and with the non-singular method (Figure 13).

27
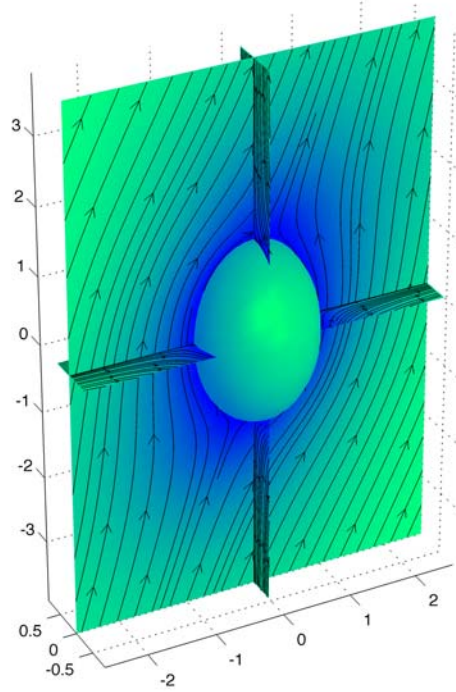
Figure 10: Streamlines of the solution with $\theta = \theta^8$ and $\lambda = 1.5$.

$18\theta/\pi$	$n = 91$	$n = 231$	$n = 325$	$n = 435$	$n = 561$
1	$1.66 \cdot 10^{-2}\,\%$	$1.35 \cdot 10^{-4}\,\%$	$9.54 \cdot 10^{-5}\,\%$	$6.16 \cdot 10^{-4}\,\%$	$3.88 \cdot 10^{-5}\,\%$
2	$1.64 \cdot 10^{-2}\,\%$	$1.64 \cdot 10^{-4}\,\%$	$9.40 \cdot 10^{-5}\,\%$	$6.12 \cdot 10^{-4}\,\%$	$4.15 \cdot 10^{-5}\,\%$
3	$1.59 \cdot 10^{-2}\,\%$	$2.28 \cdot 10^{-4}\,\%$	$8.97 \cdot 10^{-5}\,\%$	$5.97 \cdot 10^{-4}\,\%$	$4.83 \cdot 10^{-5}\,\%$
4	$1.51 \cdot 10^{-2}\,\%$	$3.01 \cdot 10^{-4}\,\%$	$8.28 \cdot 10^{-5}\,\%$	$5.74 \cdot 10^{-4}\,\%$	$5.73 \cdot 10^{-5}\,\%$
5	$1.41 \cdot 10^{-2}\,\%$	$3.71 \cdot 10^{-4}\,\%$	$7.34 \cdot 10^{-5}\,\%$	$5.45 \cdot 10^{-4}\,\%$	$6.67 \cdot 10^{-5}\,\%$
6	$1.29 \cdot 10^{-2}\,\%$	$4.33 \cdot 10^{-4}\,\%$	$6.19 \cdot 10^{-5}\,\%$	$5.12 \cdot 10^{-4}\,\%$	$7.54 \cdot 10^{-5}\,\%$
7	$1.17 \cdot 10^{-2}\,\%$	$4.84 \cdot 10^{-4}\,\%$	$4.86 \cdot 10^{-5}\,\%$	$4.79 \cdot 10^{-4}\,\%$	$8.27 \cdot 10^{-5}\,\%$
8	$1.05 \cdot 10^{-2}\,\%$	$5.22 \cdot 10^{-4}\,\%$	$3.42 \cdot 10^{-5}\,\%$	$4.50 \cdot 10^{-4}\,\%$	$8.82 \cdot 10^{-5}\,\%$
9	$9.76 \cdot 10^{-3}\,\%$	$5.46 \cdot 10^{-4}\,\%$	$1.97 \cdot 10^{-5}\,\%$	$4.30 \cdot 10^{-4}\,\%$	$9.17 \cdot 10^{-5}\,\%$
10	$9.47 \cdot 10^{-3}\,\%$	$5.54 \cdot 10^{-4}\,\%$	$1.09 \cdot 10^{-5}\,\%$	$4.23 \cdot 10^{-4}\,\%$	$9.28 \cdot 10^{-5}\,\%$

Table 2: Spheroid ratio $\lambda = 1.00$. E_F^i for different angles θ^i across the vertical directions, and for different numbers of control points across the horizontal direction, using non-singular integration method, based on 8 points Gauss quadrature.

In the non-singular method, the error $\max_i |\boldsymbol{E}_F^i|$ does not seem to have a clear convergence rate, although it is consistently lower than both Lachat Watson method and Telles method. In view of the considerations made in Section 7.2, this is not surprising, since both the Telles method and the nonsingular one reach a level of accuracy which

28

$18\theta/\pi$	$n = 91$	$n = 231$	$n = 325$	$n = 435$	$n = 561$
1	$2.16 \cdot 10^{-2}\,\%$	$3.49 \cdot 10^{-3}\,\%$	$1.49 \cdot 10^{-3}\,\%$	$6.42 \cdot 10^{-4}\,\%$	$1.76 \cdot 10^{-4}\,\%$
2	$2.19 \cdot 10^{-2}\,\%$	$3.45 \cdot 10^{-3}\,\%$	$1.48 \cdot 10^{-3}\,\%$	$6.42 \cdot 10^{-4}\,\%$	$1.74 \cdot 10^{-4}\,\%$
3	$2.27 \cdot 10^{-2}\,\%$	$3.33 \cdot 10^{-3}\,\%$	$1.44 \cdot 10^{-3}\,\%$	$6.42 \cdot 10^{-4}\,\%$	$1.67 \cdot 10^{-4}\,\%$
4	$2.39 \cdot 10^{-2}\,\%$	$3.13 \cdot 10^{-3}\,\%$	$1.38 \cdot 10^{-3}\,\%$	$6.42 \cdot 10^{-4}\,\%$	$1.55 \cdot 10^{-4}\,\%$
5	$2.54 \cdot 10^{-2}\,\%$	$2.85 \cdot 10^{-3}\,\%$	$1.29 \cdot 10^{-3}\,\%$	$6.42 \cdot 10^{-4}\,\%$	$1.39 \cdot 10^{-4}\,\%$
6	$2.69 \cdot 10^{-2}\,\%$	$2.50 \cdot 10^{-3}\,\%$	$1.19 \cdot 10^{-3}\,\%$	$6.42 \cdot 10^{-4}\,\%$	$1.19 \cdot 10^{-4}\,\%$
7	$2.84 \cdot 10^{-2}\,\%$	$2.09 \cdot 10^{-3}\,\%$	$1.08 \cdot 10^{-3}\,\%$	$6.42 \cdot 10^{-4}\,\%$	$9.38 \cdot 10^{-5}\,\%$
8	$2.96 \cdot 10^{-2}\,\%$	$1.67 \cdot 10^{-3}\,\%$	$9.77 \cdot 10^{-4}\,\%$	$6.42 \cdot 10^{-4}\,\%$	$6.54 \cdot 10^{-5}\,\%$
9	$3.03 \cdot 10^{-2}\,\%$	$1.30 \cdot 10^{-3}\,\%$	$8.99 \cdot 10^{-4}\,\%$	$6.42 \cdot 10^{-4}\,\%$	$3.48 \cdot 10^{-5}\,\%$
10	$3.06 \cdot 10^{-2}\,\%$	$1.15 \cdot 10^{-3}\,\%$	$8.70 \cdot 10^{-4}\,\%$	$6.42 \cdot 10^{-4}\,\%$	$1.13 \cdot 10^{-5}\,\%$

Table 3: Spheroid ratio $\lambda = 1.50$. E_F^i for different angles θ^i across the vertical directions, and for different numbers of control points across the horizontal direction, using non-singular integration method, based on 8 points Gauss quadrature.

$18\theta/\pi$	$n = 91$	$n = 231$	$n = 325$	$n = 435$	$n = 561$
1	$1.75 \cdot 10^{-2}\,\%$	$2.45 \cdot 10^{-4}\,\%$	$3.41 \cdot 10^{-4}\,\%$	$1.70 \cdot 10^{-4}\,\%$	$7.31 \cdot 10^{-4}\,\%$
2	$1.73 \cdot 10^{-2}\,\%$	$7.91 \cdot 10^{-4}\,\%$	$3.39 \cdot 10^{-4}\,\%$	$1.79 \cdot 10^{-4}\,\%$	$7.24 \cdot 10^{-4}\,\%$
3	$1.68 \cdot 10^{-2}\,\%$	$1.52 \cdot 10^{-3}\,\%$	$3.34 \cdot 10^{-4}\,\%$	$2.04 \cdot 10^{-4}\,\%$	$7.00 \cdot 10^{-4}\,\%$
4	$1.60 \cdot 10^{-2}\,\%$	$2.24 \cdot 10^{-3}\,\%$	$3.24 \cdot 10^{-4}\,\%$	$2.40 \cdot 10^{-4}\,\%$	$6.61 \cdot 10^{-4}\,\%$
5	$1.47 \cdot 10^{-2}\,\%$	$2.93 \cdot 10^{-3}\,\%$	$3.12 \cdot 10^{-4}\,\%$	$2.80 \cdot 10^{-4}\,\%$	$6.05 \cdot 10^{-4}\,\%$
6	$1.32 \cdot 10^{-2}\,\%$	$3.57 \cdot 10^{-3}\,\%$	$2.96 \cdot 10^{-4}\,\%$	$3.20 \cdot 10^{-4}\,\%$	$5.33 \cdot 10^{-4}\,\%$
7	$1.13 \cdot 10^{-2}\,\%$	$4.13 \cdot 10^{-3}\,\%$	$2.79 \cdot 10^{-4}\,\%$	$3.57 \cdot 10^{-4}\,\%$	$4.47 \cdot 10^{-4}\,\%$
8	$9.36 \cdot 10^{-3}\,\%$	$4.57 \cdot 10^{-3}\,\%$	$2.63 \cdot 10^{-4}\,\%$	$3.87 \cdot 10^{-4}\,\%$	$3.52 \cdot 10^{-4}\,\%$
9	$7.72 \cdot 10^{-3}\,\%$	$4.85 \cdot 10^{-3}\,\%$	$2.52 \cdot 10^{-4}\,\%$	$4.06 \cdot 10^{-4}\,\%$	$2.68 \cdot 10^{-4}\,\%$
10	$7.04 \cdot 10^{-3}\,\%$	$4.95 \cdot 10^{-3}\,\%$	$2.47 \cdot 10^{-4}\,\%$	$4.13 \cdot 10^{-4}\,\%$	$2.30 \cdot 10^{-4}\,\%$

Table 4: Spheroid ratio $\lambda = 2.00$. E_F^i for different angles θ^i across the vertical directions, and for different numbers of control points across the horizontal direction, using non-singular integration method, based on 8 points Gauss quadrature.

is lower than the error in the representation of the normal, and further improvement cannot be achieved.

For all considered geometries and combination of collocation points, the computed error with the non-singular method is between $10^{-2}\%$ and $10^{-4}\%$ for the quadratic case and between $10^{-3}\%$ and $10^{-4}\%$ for the cubic case at a fraction of the computational cost (see Figure 9). The error obtained with the Lachat Watson technique is about two orders of magnitude worse of both the Telles and the non-singular case, at a much higher computational cost.

Figure 11 seems to suggest that the simplistic implementation we made of the Lachat Watson technique is not a suitable choice for IGA-BEM implementations of stokes flows. As kindly suggested by one of the reviewers, it seems that eight quadrature points on both the radial and angle direction are not enough to reach satisfactory convergence results with this technique, and a higher number of quadrature points should be used in the angle direction. The additional computational cost associated with this choice, however, makes it a less appealing solution if compared with Telles transformation or
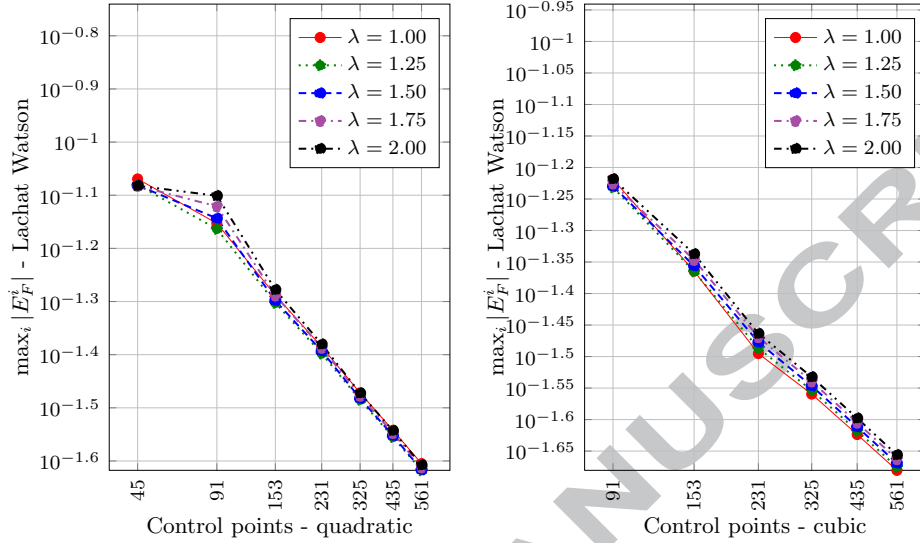
29

Figure 11: Maximum error E_F^i across all angles θ^i, for different number of control points, with quadratic NURBS (left) and with cubic NURBS (right), using Lachat Watson quadrature rules based on 8 points Gauss quadrature.
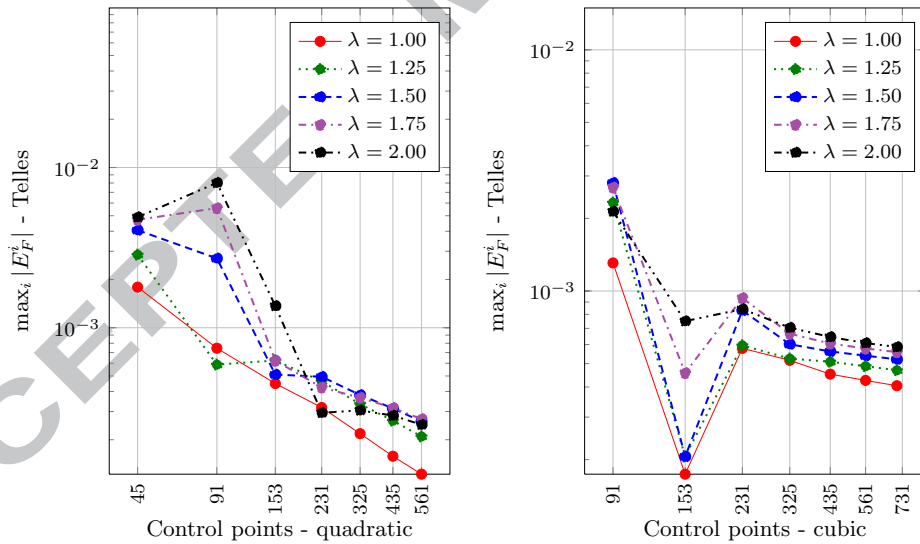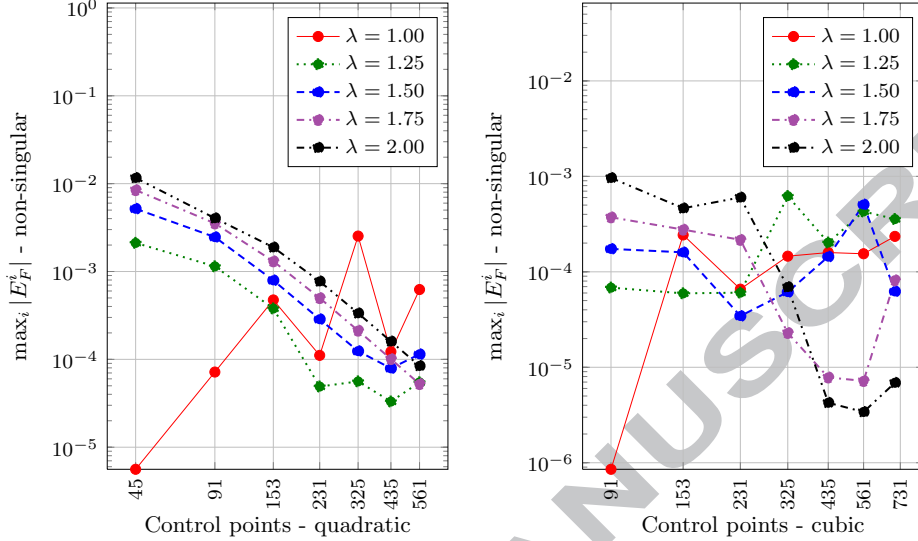

Figure 12: Maximum error E_F^i across all angles θ^i, for different number of control points, with quadratic NURBS (left) and with cubic NURBS (right), using Telles quadrature rules based on 8 points Gauss quadrature.

30

Figure 13: Maximum error E_F^i across all angles θ^i, for different number of control points, with quadratic NURBS (left) and with cubic NURBS (right), using non-singular quadrature rules based on 8 points Gauss quadrature.

with the nonsingular technique introduced in Section 6.

Figures 12 and 13 show that both Telles and the non-singular method presented in this paper are suitable choices for accurate IGA-BEM approximations of Stokes flow, since both methods reach a level of accuracy which is comparable with the error in the approximation of the normal vector field $\boldsymbol{n}$, presented in Figure 7.

Comparing the behaviour of the quadratic approximations versus the cubic ones in Figures 11, 12 and 13 seems to suggest that using p refinement would lead to much lower values of the error while keeping the same number of control points (see, for example [9]). This, however, requires a careful treatment of the quadrature rules to ensure that the higher polynomial degree in both the geometry and finite dimensional space is matched by higher regularity in the integration formulas in order to fully benefit from higher order convergences.

For the case $\theta = 0$, we asses the convergence of all methods in the L^2 norm using the analytical solution. Given a unit velocity field directed along the axis of symmetry, the analytical solution for the normal stress density $\boldsymbol{\sigma}\boldsymbol{n} = \boldsymbol{f} = f_z\boldsymbol{e}_z$ is directed along the z axis and is given by:

$$f_z = 2\frac{e^3}{(1-e^2)^{1/6}\left(\frac{1+e^2}{2}\ln\left(\frac{1+e}{1-e}\right)-e\right)}\frac{1}{\sqrt{1-e^2z^2/b^2}}. \tag{84}$$

In Figures 14, 15 and 16 we present the plot of the error in the L^2 norm of the normal stress density $\boldsymbol{f}$ during k refinement for quadratic and cubic NURBS for all considered methods.
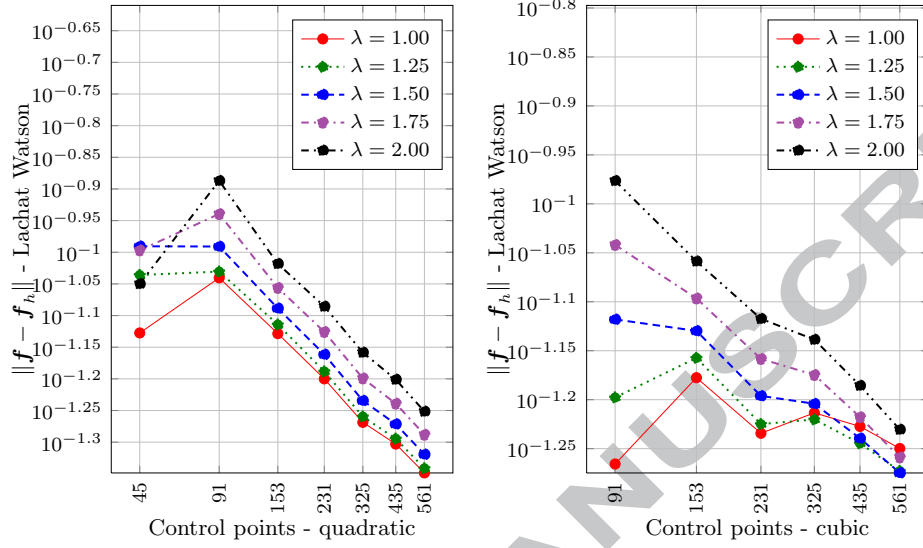
31

Figure 14: L^2 error for different number of control points, with quadratic NURBS (left) and with cubic NURBS (right), using Lachat Watson integration method, based on 8 points Gauss quadrature.
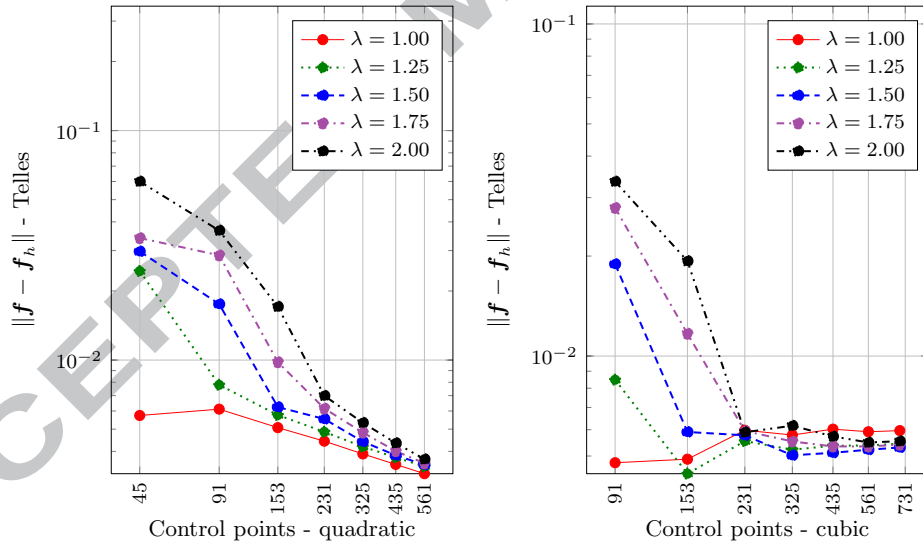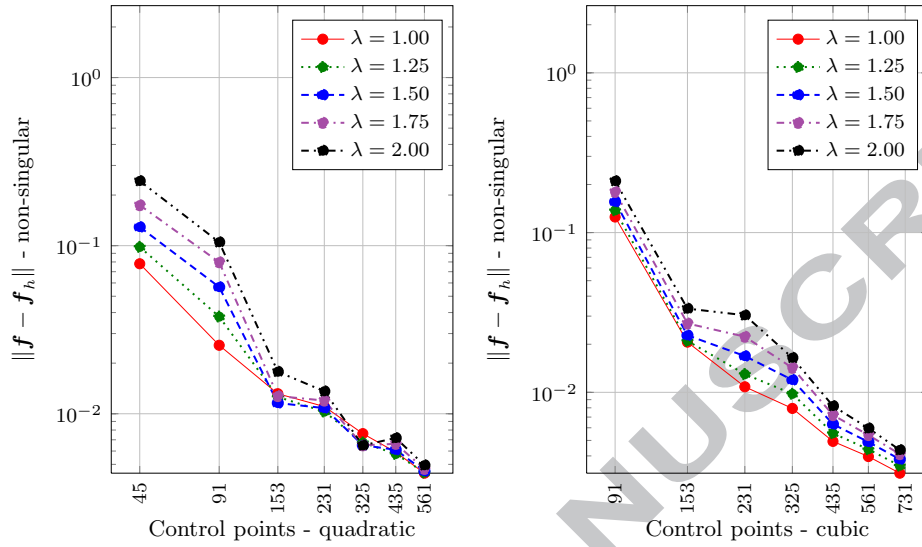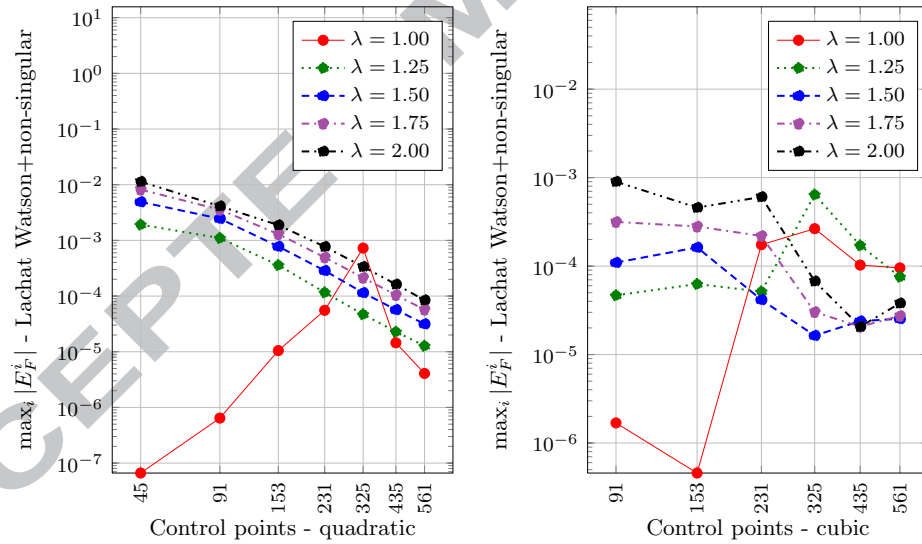

Figure 15: L^2 error for different number of control points, with quadratic NURBS (left) and with cubic NURBS (right), using Telles integration method, based on 8 points Gauss quadrature.

The technique introduced in Section 6 is independent on the quadrature rules which are used to integrate the boundary integral equations, and can be used also with standard

32

Figure 16: L^2 error for different number of control points, with quadratic NURBS (left) and with cubic NURBS (right), using non-singular integration method, based on 8 points Gauss quadrature.
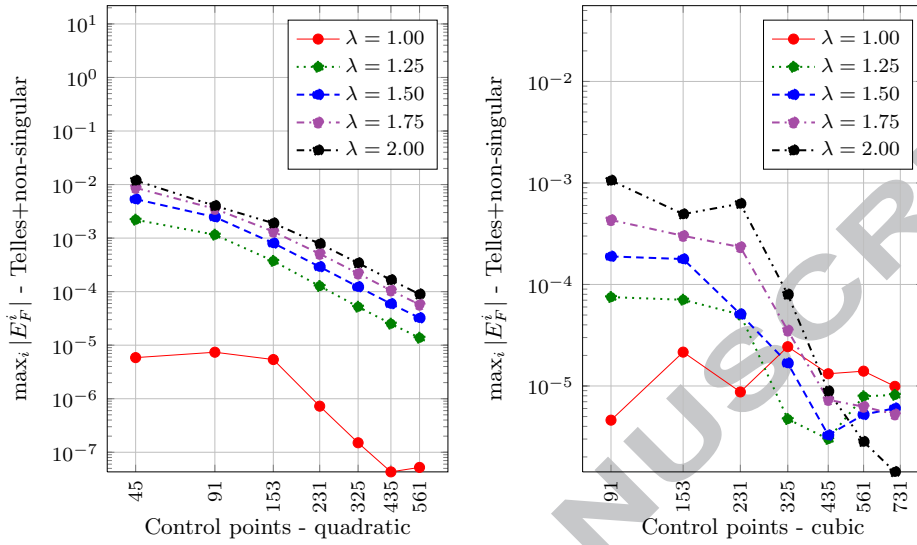

Figure 17: Maximum error E_F^i across all angles θ^i, for different number of control points, with quadratic NURBS (left) and with cubic NURBS (right), using Lachat Watson+non-singular quadrature rules based on 8 points Gauss quadrature.

integration techniques.

In Figures 17 and 18 we plot the error $\max_i |\boldsymbol{E}_F^i|$ when using a combination of the non-

33

Figure 18: Maximum error E_F^i across all angles θ^i, for different number of control points, with quadratic NURBS (left) and with cubic NURBS (right), using Telles+non-singular quadrature rules based on 8 points Gauss quadrature.
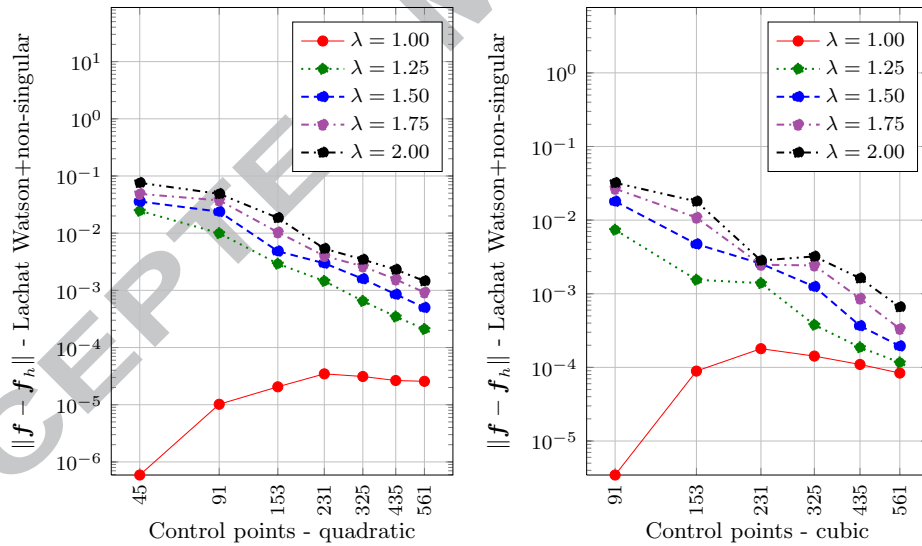

Figure 19: L^2 error for different number of control points, with quadratic NURBS (left) and with cubic NURBS (right), using Lachat Watson+non-singular integration method, based on 8 points Gauss quadrature.
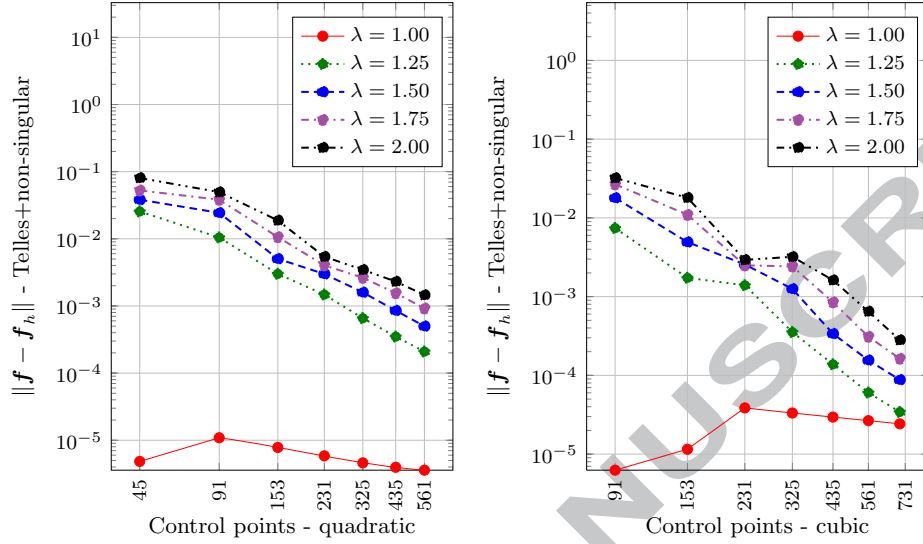
34

Figure 20: L^2 error for different number of control points, with quadratic NURBS (left) and with cubic NURBS (right), using Telles+non-singular integration method, based on 8 points Gauss quadrature.

singular integration technique of Section 6 with the Lachat Watson and Telles quadrature techniques. Comparing the results with Figures 11, and 12 we observe a drastic improvement on the error, with a negligible additional computational cost.

In Figure 19 and 20 we plot the error in the L^2 norm when combining our technique with the classical ones.

When used as a standalone method, the desingularization technique (Figures 13 and 16) follows very closely the error in the representation of the normal (Figure 7), which was argued to be an intrinsic limit of the finite dimensional space V_h (Section 7.2). Telles method (Figures 12 and 15), on the other hand, seems to reach the limit of the geometrical error slightly faster with respect to the nonsingular technique. The higher accuracy, however, is reached at a much higher computational cost (Figure 9), which is one order of magnitude higher than the cost associated to the nonsingular technique.

The best results in terms of accuracy are obtained when one combines our desingularization technique with one of the standard quadrature techniques, as in the cases LW+NS and T+NS (Figures 17–20). The method we propose can be successfully used to tackle IGA-BEM problems, both as a standalone method with classical Gauss quadrature rules, as well as in combination with integration techniques typical of BEM implementations, such as the Lachat Watson technique or the Telles one.

8. Conclusions

Isogeometric boundary element methods for Stokes flow are very promising in terms of accuracy, and produce consistently better results than the standard boundary element method. We find that the nonsingular IGA-BEM based on quadratic NURBS achieves

35

an accuracy which is around $10^{-3}\%$ already with 231 nodes in a set of problems reported in [43], where 642 nodes were necessary for an accuracy of about .5% (more than one order higher).

The method proposed in this paper extends the ideas of Klaseboer et al. [27, 26, 43] to isogeometric boundary element methods (IGA-BEM). The main advantage of this approach comes from the true desingularization of the boundary integral equations, thanks to which it is possible to use standard quadrature formulas to assemble the system matrices. A model problem for three dimensional Stokes flows was presented, showing very good agreement with known analytical solutions. Although the superior convergence properties of IGA-BEM is evident, a deeper investigation on the quadrature formulas is desirable, in order to fully exploit the potential of isogeometric analysis (see, for example, [7]).

The non-singular technique presented in this paper delivers approximation properties which are similar both qualitatively and quantitatively to the ones obtained with Telles algorithm, at a fraction of the computational cost. Moreover, it outclasses another classical method which is often used in standard BEM implementations (the Lachat Watson technique) but which fails to deliver satisfactory results in the iso-geometric context, unless one is willing to pay a much higher computational cost.

Although we could not observe clear L^2 convergence rates in the examples we presented, we believe that these results depend mostly on the approximation properties of the iso-geometric finite dimensional spaces, which lack the capability to represent exactly the outer normals. Despite this fact, the combination of the non-singular method with standard singular integration techniques, yields a significant increase both in accuracy and robustness of standard IGA-BEM methods.

In [32] and [30] it is argued that this kind of regularization of the boundary integral integrations requires the boundary Γ to be of class C^1. We are currently investigating the convergence properties of both the regularization presented in Section 6 and of standard IGA-BEM techniques when applied to geometries which contain corners and edges.

We are planning applications of the method proposed in this paper to model full three-dimensional flows induced by swimming bacteria and unicellular organisms, extending [1, 4, 3, 2, 6] and to model the relaxation dynamics and the flow around three-dimensional lipid bilayer membranes, extending [5, 38]. The flexibility and the accuracy of the nonsingular IGA-BEM makes it also a good candidate to replace or complement more complex fluid-structure interaction methods, such as the ones presented in [34, 21, 11].

Acknowledgements

The authors are grateful to the anonymous reviewers for their helpful comments.

References

[1] F. Alouges, A. DeSimone, and L. Heltai. Numerical strategies for stroke optimization of axisymmetric microswimmers. *Mathematical Models and Methods in Applied Science*, 21(02):361–387, 2011.

[2] F. Alouges, A. DeSimone, and L. Heltai. Optimally swimming stokesian robots. *Discrete and Continuous Dynamical Systems - Series B (DCDS-B)*, 18(5):11891215, 2013.

[3] F. Alouges, A. DeSimone, and A. Lefebvre. Optimal strokes for low Reynolds number swimmers: an example. *J. Nonlinear Sci.*, 18(3):277–302, 2008.

[4] F. Alouges, A. DeSimone, and A. Lefebvre. Optimal strokes for axisymmetric microswimmers. *The European Physical Journal E*, 28(3):279–284, mar 2009.

[5] M. Arroyo and A. DeSimone. Relaxation dynamics of fluid membranes. *Physical Review E*, 79(3):031915, 2009.

[6] M. Arroyo, L. Heltai, D. Millán, and A. DeSimone. Reverse engineering the euglenoid movement. *Proceedings of the National Academy of Sciences*, 109(44):17874–17879, 2012.

[7] F. Auricchio, F. Calabrò, T. Hughes, A. Reali, and G. Sangalli. A simple algorithm for obtaining nearly optimal quadrature rules for nurbs-based isogeometric analysis. *Computer Methods in Applied Mechanics and Engineering*, 2012.

[8] F. Auricchio, L. da Veiga, T. Hughes, A. Reali, and G. Sangalli. Isogeometric collocation methods. *Mathematical Models and Methods in Applied Sciences*, 20(11):2075–2107, 2010.

[9] L. Beirão da Veiga, A. Buffa, J. Rivas, and G. Sangalli. Some estimates for h–p–k-refinement in isogeometric analysis. *Numerische Mathematik*, 118(2):271–305, 2011.

[10] K. Belibassakis, T. Gerostathis, K. Kostas, C. Politis, P. Kaklis, A. Ginnis, and C. Feurer. A bem-isogeometric method with application to the wavemaking resistance problem of ships at constant speed. In *30th International Conference on Offshore Mechanics and Arctic Engineering, OMAE2011, Rotterdam, The Netherlands*, pages 95 – 102, 2011.

[11] D. Boffi, L. Gastaldi, L. Heltai, and C. S. Peskin. On the hyper-elastic formulation of the immersed boundary method. *Computer Methods in Applied Mechanics and Engineering*, 197(25-28):2210–2231, 2008.

[12] A. Buffa, C. De Falco, and G. Sangalli. Isogeometric analysis: stable elements for the 2d stokes equation. *International Journal for Numerical Methods in Fluids*, 65(11-12):1407–1422, 2011.

[13] A. Chwang and T. Wu. Hydromechanics of low-reynolds-number flow. part 2. singularity method for stokes flows. *J. Fluid Mech*, 67(Part 4):787, 1975.

[14] J. Cottrell, T. Hughes, and Y. Bazilevs. *Isogeometric analysis: toward integration of CAD and FEA*. John Wiley & Sons Inc, 2009.

[15] P. Crosetto, P. Reymond, S. Deparis, D. Kontaxakis, N. Stergiopulos, and A. Quarteroni. Fluid–structure interaction simulation of aortic blood flow. *Computers & Fluids*, 43(1):46–57, 2011.

[16] T. Cruse. An improved boundary-integral equation method for three dimensional elastic stress analysis. *Computers & Structures*, 4(4):741–754, 1974.

[17] R. Dautray and J.-L. Lions. *Mathematical analysis and numerical methods for science and technology*. Springer, 2000.

[18] C. de Falco, A. Reali, and R. Vázquez. Geopdes: A research tool for isogeometric analysis of pdes. *Advances in Engineering Software*, 42(12):1020–1034, 2011.

[19] T. Greville. Numerical procedures for interpolation by spline functions. *Journal of the Society for Industrial & Applied Mathematics, Series B: Numerical Analysis*, 1(1):53–68, 1964.

[20] J. Gu, J. Zhang, X. Sheng, and G. Li. B-spline approximation in boundary face method for three-dimensional linear elasticity. *Engineering Analysis with Boundary Elements*, 35(11):1159 – 1167, 2011.

[21] L. Heltai and F. Costanzo. Variational implementation of immersed finite element methods. *Computer Methods in Applied Mechanics and Engineering*, 229–232(0):110 – 127, 2012.

[22] G. C. Hsiao and W. L. Wendland. *Boundary integral equations*, volume 164 of *Applied Mathematical Sciences*. Springer-Verlag, Berlin, 2008.

[23] Q. Huang and T. Cruse. Some notes on singular integral techniques in boundary element analysis. *International Journal for Numerical Methods in Engineering*, 36(15):2643–2659, 1993.

[24] T. Hughes, J. Cottrell, and Y. Bazilevs. Isogeometric analysis: CAD, finite elements, NURBS, exact geometry and mesh refinement. *Computer Methods in Applied Mechanics and Engineering*, 194(39-41):4135–4195, 2005.

[25] G. Kim, C. Lee, and J. Kerwin. A b-spline based higher order panel method for analysis of steady flow around marine propellers. *Ocean Engineering*, 34(14):2045–2060, 2007.

[26] E. Klaseboer, C. Fernandez, and B. Khoo. A note on true desingularisation of boundary integral methods for three-dimensional potential problems. *Engineering Analysis with Boundary Elements*, 33(6):796–801, 2009.

[27] E. Klaseboer, Q. Sun, and D. Chan. Non-singular boundary integral methods for fluid mechanics applications. *Journal of Fluid Mechanics*, 696(1):468–478, 2012.

[28] J. Lachat and J. Watson. Effective numerical treatment of boundary integral equations: A formulation for three-dimensional elastostatics. *International Journal for Numerical Methods in Engineering*, 10(5):991–1005, 2005.

[29] K. Li and X. Qian. Isogeometric analysis and shape optimization via boundary integral. *Computer-Aided Design*, 43(11):1427 – 1437, 2011.

[30] Y. Liu. On the simple-solution method and non-singular nature of the bie / bem - a review and some new results. *Engineering analysis with boundary elements*, 24:789795, 2000.

[31] Y. Liu and N. Nishimura. The fast multipole boundary element method for potential problems: a tutorial. *Engineering Analysis with Boundary Elements*, 30(5):371–381, 2006.

[32] Y. J. Liu and T. J. Rudolphi. New identities for fundamental solutions and their applications to non-singular boundary element formulations. *Computational Mechanics*, 24(4):286292, Oct 1999.

[33] MATLAB. *Version 8.0.0.783 (R2012b)*. The MathWorks Inc., Natick, Massachusetts, 2012.

[34] A. Mola, L. Heltai, and A. DeSimone. A stable and adaptive semi-lagrangian potential model for unsteady and nonlinear ship-wave interactions. *Engineering Analysis with Boundary Elements*, 37(1):128 – 143, 2013.

[35] L. Piegl and W. Tiller. *The NURBS book (2nd ed.)*. Springer-Verlag New York, Inc., New York, NY, USA, 1997.

[36] C. Politis, A. I. Ginnis, P. D. Kaklis, K. Belibassakis, and C. Feurer. An isogeometric bem for exterior potential-flow problems in the plane. In *2009 SIAM/ACM Joint Conference on Geometric and Physical Modeling*, SPM '09, pages 349–354, New York, NY, USA, 2009. ACM.

[37] C. Pozrikidis. *Boundary integral and singularity methods for linearized viscous flow*. Cambridge Texts in Applied Mathematics. Cambridge University Press, Cambridge, 1992.

[38] M. Rahimi and M. Arroyo. Shape dynamics, lipid hydrodynamics, and the complex viscoelasticty of bilayer membranes. *Physical Review E*, 86(1):011932, 2012.

[39] V. Rokhlin. Rapid solution of integral equations of classical potential theory. *Journal of Computational Physics*, 60(2):187–207, 1985.

[40] R. Simpson, S. Bordas, J. Trevelyan, and T. Rabczuk. A two-dimensional isogeometric boundary element method for elastostatic analysis. *Computer Methods in Applied Mechanics and Engineering*, 2011.

[41] M. Spink. Nurbs toolbox, 2000.

[42] O. Steinbach. *Numerical approximation methods for elliptic boundary value problems: finite and boundary elements*. Springer Verlag, 2008.

[43] Q. Suna, E. Klaseboerb, B. Khooa, and D. Chana. Implementation of a well-conditioned boundary integral method for stokes flow and elastostatic problems. Submitted to Journal of Computational Physics.

[44] T. Takahashi and T. Matsumoto. An application of fast multipole method to isogeometric boundary element method for laplace equation in two dimensions. *Engineering Analysis with Boundary Elements*, 36(12):1766 – 1775, 2012.

[45] J. Telles. A self-adaptive co-ordinate transformation for efficient numerical evaluation of general boundary element integrals. *International Journal for Numerical Methods in Engineering*, 24(5):959–973, 2005.